

www.acsanm.org Article

# Eradication of Fungi Using MoSe<sub>2</sub>/Chitosan Nanosheets

Sanchari Saha, Matthew S. Gilliam, Qing Hua Wang,\* and Alexander A. Green\*



Cite This: ACS Appl. Nano Mater. 2022, 5, 133-148



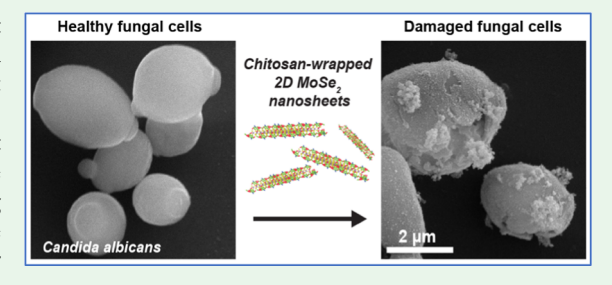
**ACCESS** I

Metrics & More

Article Recommendations

SI Supporting Information

**ABSTRACT:** Antifungal drug resistance is an increasingly significant threat to humans, livestock, and crops. Recent studies have shown nanomaterials as promising alternatives in combating drug-resistant pathogens. Here, we show that molybdenum diselenide (MoSe<sub>2</sub>) nanosheets dispersed in the cationic polymer chitosan (CS) exhibit exceptional antifungal activity. The MoSe<sub>2</sub>/CS nanosheets provide minimum inhibitory concentrations (MICs) between 0.78 and 37.5  $\mu$ g ml<sup>-1</sup> against a variety of unicellular fungal strains and demonstrate minimum fungicidal concentrations (MFCs) from 0.5 to 75  $\mu$ g ml<sup>-1</sup> for diverse unicellular and filamentous strains. Furthermore, we demonstrate



the ability of  $MoSe_2/CS$  to eradicate increasingly prevalent and highly multi-drug-resistant (MDR) fungi Candida auris strains with MICs of 25 to 50  $\mu$ m ml<sup>-1</sup> and MFCs of 37.5 to 150  $\mu$ m ml<sup>-1</sup>. The effective antifungal activity of  $MoSe_2/CS$  was observed after an incubation time of 3 h, which is faster than the time needed for other nanomaterial-based antifungal agents incorporating graphene, two-dimensional (2D) nanomaterials, or silver nanoparticles.  $MoSe_2/CS$  also showed high biocompatibility and was benign toward human red blood cells and human embryonic kidney cells. Electron microscopy and confocal optical microscopy show that fungal cells treated with  $MoSe_2/CS$  nanosheets exhibit morphological deformities, ruptured cell walls and interior voids, and metabolic inactivation. Mechanistic investigations revealed that treatment with  $MoSe_2/CS$  triggers complete membrane depolarization and membrane disintegration within 3 h. Hence, this work demonstrates that the biocompatible nanomaterial  $MoSe_2/CS$  is a highly effective alternative antifungal agent against many kinds of pathogenic fungi including MDR strains.

KEYWORDS: antifungal materials, 2D materials, multi-drug-resistant fungi, Candida auris, antifungal mechanism

### **■ INTRODUCTION**

Fungal diseases have emerged as one of the major global threats to human health and can lead to considerable economic losses. The treatment of fungal diseases is increasingly challenging due to growing antifungal drug resistance,3 resulting in high mortality rates.4 Recently, fungal diseases have infected more than a billion patients per year worldwide, leading to more than 1.5 million fatalities. 1,2,4 Recent estimates have found worldwide annual case counts of ~3 million for chronic pulmonary aspergillosis, ~223,100 for cryptococcal meningitis complicating HIV/AIDS, ~700,000 for invasive candidiasis, ~250,000 for invasive aspergillosis, and over 10 million for fungal asthma.<sup>5</sup> Fungal diseases that attack plants lead to significant harm to agriculture and farming,6 while those that attack animals threaten many species. Overall, it is estimated that approximately 65% of pathogen-driven host loss is caused by fungi that threaten animal-host and plant-host species.8 Furthermore, climate change has accelerated the growth of fungal diseases. Candida auris (C. auris) is a new species of yeast that has been associated with outbreaks in hospitals around the world, 10 although it was only first discovered in Japan in 2009.11 It is causing substantial alarm due to its worldwide spread, its propensity for outbreaks in hospitals and clinics, and its resistance toward enhanced infection prevention and control (IPC) measures. 12 C. auris tends to infect critically ill patients

and is increasingly resistant to common antifungal drugs with higher minimum inhibitory concentrations (MICs) than usual, <sup>13</sup> leading to its designation as multi-drug-resistant (MDR). <sup>12,14,15</sup> Current therapeutics to treat fungal diseases have significant limitations against MDR fungi, and novel therapeutic alternatives are promptly needed. <sup>16</sup>

Currently, the primary drugs available to treat fungal infections are limited to amphotericin B, azoles, echinocandins, and 5-flucytosine. However, pathogenic fungi have several well-characterized resistance mechanisms, leading to the gradual inefficacy of these drugs. <sup>16–20</sup> Although researchers are investigating novel ways to target these resistant fungal pathogens, they are evolving and growing new resistant genes at a much faster rate. <sup>1</sup> Hence, alternative approaches are needed to strengthen the antifungal pipeline. <sup>1</sup> In recent years, nanomaterials have been used to form novel antimicrobial agents with distinctive chemical and physical properties. <sup>16,21</sup> Nanomaterials like silver (Ag), <sup>21,22</sup> zinc oxide (ZnO), <sup>23</sup>

Received: April 13, 2021 Accepted: January 4, 2022 Published: January 17, 2022





titanium dioxide  $(TiO_2)$ ,  $^{23}$  iron oxide  $(Fe_3O_4)$ ,  $^{24}$  copper oxide (CuO),  $^{25}$  magnesium oxide (MgO),  $^{26}$  and nitric oxide (NO) nanoparticles  $^{27}$  have displayed antibacterial activity. However, their toxicity has proven to be challenging for applications in the biomedical field.  $^{28}$ 

There have been numerous studies in the literature on using a variety of nanostructured materials as antifungal agents. Onedimensional (1D) single-walled carbon nanotubes (SWCNTs) were able to kill Fusarium graminearum and Fusarium poae but at very high concentrations of 500 μg ml<sup>-1</sup> with less than 96% killing efficiency.<sup>29</sup> However, SWCNTs conjugated with antifungal drugs like amphotericin B showed relatively good killing efficiency at 80  $\mu$ g ml<sup>-1</sup> against Candida albicans.<sup>30</sup> Twodimensional (2D) nanomaterials have been studied by many groups for their antimicrobial effects over the past decade.<sup>3</sup> Carbon-based nanomaterials (CBNs), which include graphene and graphene oxide, have been studied extensively for their antimicrobial properties. 32,33 They exhibit high mechanical strengths, large surface-to-volume ratios, and prominent physicochemical properties when bacteria are treated by them.<sup>34</sup> Recently, transition-metal dichalcogenides (TMDCs) have also shown unique potential in biomedical applications. 35,36 In particular, they have exhibited great promise in antimicrobial activity due to their large surface area, hydrophobicity, and high biocompatibility, which are attributed to their 2D structure and better biocompatibility compared to CBNs. 30,36-43 Molybdenum disulfide (MoS<sub>2</sub>) modified with chitosan (CS) and silver nanoparticles (MoS2-CS-AgNPs) was able to inhibit the growth of plant fungi Saccharomyces uvarum and Aspergillus niger at low concentrations of 6.8 and 4.2  $\mu$ g ml<sup>-1</sup>, respectively, but only after long incubation times of 72 h.<sup>36</sup> A nanocomposite of AgNPs coupled with zinc oxide (Ag@ZnO) showed complete killing (MFC) of Candida krusei at 250 µg ml<sup>-1</sup> after 18 h of incubation. 44 Recently, our group conducted a detailed study of liquid exfoliated TMDC nanosheets encapsulated in synthetic single-stranded DNA and found that molybdenum diselenide (MoSe<sub>2</sub>) showed excellent antibacterial efficiency against many strains of MDR bacteria.<sup>45</sup>

However, there have been relatively few studies on the antifungal potential of TMDCs. 36,46-48 At the same time, developing and using biological materials against increasingly drug-resistant microbes is gaining in interest. 49,50 Chitosan (CS) is a cationic polysaccharide that is nontoxic, biocompatible, and biodegradable since it is derived from the shells of crustaceans and has diverse therapeutic properties including antimicrobial activity. 36,38,51 CS has been known to inhibit mRNA synthesis once it enters the cell cytoplasm, thus triggering cell death and making it an effective antifungal agent. Because CS is positively charged, it can interact electrostatically with the negatively charged fungal cell wall, making it highly target-specific, and it can increase the permeability of cell membranes, causing leakage of the cytoplasm. Chitosan is also able to bind with trace elements as a chelating agent, thereby inhibiting fungal cell growth. 52,53 Previous studies have shown that adding nanoparticles to a CS matrix can enhance antimicrobial activity while maintaining biocompatibility. 36,38,54 Thus, the combination of CS and 2D materials has excellent potential to form antifungal agents to combat pathogenic fungi.

In this paper, we report the antifungal activity of 2D MoSe<sub>2</sub> nanosheets formed by liquid phase exfoliation in a 0.5% w/v low-molecular weight (LMW) CS aqueous solution. The resulting MoSe<sub>2</sub> nanosheets are encapsulated in CS (MoSe<sub>2</sub>/CS) and exhibit exceptional antifungal activity. Moreover, they

do so without any requiring any modifications such as surface functionalization with complex ligands,  $^{36}$  biocidal nanoparticles,  $^{55}$  photosensitizers,  $^{56}$  or antifungal drugs  $^{30}$  and without needing external stimuli like near infrared (nIR) light,  $^{57}$  which has been reported in the literature. Both unicellular and filamentous fungi were successfully inhibited at low concentrations of MoSe<sub>2</sub>/CS between 37 and 75  $\mu$ g ml<sup>-1</sup>.

The physical and chemical influence of MoSe<sub>2</sub>/CS nanosheets on the cell membranes of fungal cells were investigated through a series of mechanistic studies, which showed that more than 95% of cells had membranes that were depolarized and disintegrated. High-resolution imaging via confocal scanning laser microscopy (CSLM), transmission electron microscopy (TEM), and scanning electron microscopy (SEM) were used to directly show that the outer lipid bilayers surrounding the fungal cells are physically disrupted due to interaction with the MoSe<sub>2</sub>/ CS nanosheets. Overall, there is a combined effect of membrane damage, membrane depolarization, and metabolic inactivation. The MoSe<sub>2</sub>/CS nanosheets were also used to kill several strains of the highly pathogenic and multi-drug-resistant fungus *C. auris*. Biocompatibility experiments showed that the MoSe<sub>2</sub>/CS nanosheets resulted in more than 90% viability of mammalian cells and human red blood cells in up to 75  $\mu$ g ml<sup>-1</sup> of MoSe<sub>2</sub>/ CS. These experiments combine to show that MoSe<sub>2</sub>/CS nanosheets are highly effective at killing fungi while being very biocompatible, which suggests that they may be broadly applicable in a variety of applications where antifungal performance is needed.

#### EXPERIMENTAL SECTION

Materials. Molybdenum(IV) selenide (MoSe<sub>2</sub>, 325 mesh, 99.9% trace metal basis, item number: 778087), low-molecular weight chitosan (LMW CS) (50,000-190,000 Da, 75-85% deacetylated, item number: 448869), phosphate-buffered saline solution (PBS, pH 7.4), Dulbecco's phosphate-buffered saline (DPBS), potato dextrose broth (PDB) medium, PDB agar, Dulbecco's modified Eagle's medium (DMEM), poly-L-lysine, trypsin-EDTA, and propidium iodide (PI) were purchased from Sigma-Aldrich. Glacial acetic acid, yeast malt (YM) broth, YM agar, and glutaraldehyde solution (25% in H<sub>2</sub>O) were purchased from Thomas Scientific Holdings LLC. Difco Sabouraud dextrose broth (SDB) medium and Difco SDB agar were purchased from Spectrum Chemical Mfg. Corp. Human embryonic kidney 293 cells (HEK293) were purchased from ATCC. Coomassie Brilliant Blue G-250 was purchased from Bio-Rad. Whole red blood cells (RBCs) from a single donor were purchased from Innovative Research. The alamarBlue reagent cell proliferation assay was purchased from G-Biosciences. Acetone and ethanol were purchased from VWR. Osmium tetroxide (OsO<sub>4</sub>, 98% purity) was purchased from Combi-Blocks Inc. Concavalin A, Alexa Fluor 488 conjugate (ConA), Invitrogen FUN 1 cell stain (Fun 1), and Invitrogen (bis-(1,3-dibutylbarbituric acid) trimethine oxonol) (DiBaC<sub>4</sub>) were purchased from Thermo Fisher Scientific.

Fungal Strains. Issatchenkia orientalis (I. orientalis, ATCC 6258), Saccharomyces cerevisiae (S. cerevisiae, ATCC 9763), Candida parapsilosis (C. parapsilosis, ATCC 22019), Candida albicans (C. albicans, ATCC 76485), Cryptococcus neoformans (C. neoformans, ATCC 20821), Cryptococcus gattii (C. gattii, ATCC MYA-4071), Aspergillus fumigatus (A. fumigatus ATCC, MYA-4609), Fusarium verticillioides (F. verticillioides, ATCC MYA-3629), and Fusarium falciforme (F. falciforme, ATCC MYA-3636) were purchased from ATCC. The Candida auris panel including Candida auris (C. auris, 0386), C. auris (0388), C. auris (0389), Candida duobushaemulonii (C. duobushaemulonii, 0394), Candida haemulonii (C. haemulonii, 0395), Krusei ohmeri (K. ohmeri, 0396), Candida krusei (C. krusei, 0397), Candida lusitaniae (C. lusitaniae, 0398), and Saccharomyces cerevisiae (S. cerevisiae, 0399)

were obtained from the CDC & FDA Antibiotic Resistance (AR) Isolate Bank.

Preparation of MoSe<sub>2</sub>/Chitosan Dispersions. A 0.5% w/v solution of chitosan (CS) was made by dissolving the solid polymer in 1% acetic acid. Five hundred milligrams of bulk MoSe<sub>2</sub> powder was ultrasonicated in 20 mL of 0.5% CS solution for 2 h at 25 W power using a 1/8" microtip probe in a Branson Digital Sonifier SFX 550. The sonicated sample was centrifuged at 5000 rcf for 10 min followed by centrifuging at 21,000 rcf for 5 min using an Eppendorf 5424 Microcentrifuge with a fixed angle (45°) rotor. The supernatant was then collected for subsequent experiments. For control experiments, a 0.5% CS solution was sonicated and centrifuged following the same protocol but without any MoSe<sub>2</sub>. The concentration of MoSe<sub>2</sub> was obtained using inductively coupled plasma mass spectrometry (ICP-MS). Liquid dispersions for ICP-MS analysis were first acidified in nitric acid overnight and diluted to 2 wt % concentration of nitric acid. The samples were then analyzed by a Thermo Fisher iCap Q quadrupole instrument.

Characterization and Imaging. Absorbance (UV-Vis) spectra for the dispersed 2D MoSe<sub>2</sub>/CS and CS alone were acquired using a Jasco V-670 Spectrophotometer. The samples were loaded in a quartz cell with a 1.0 cm path length. Samples for transmission electron microscopy (TEM) imaging were prepared by drop-casting 10  $\mu$ L of the diluted MoSe<sub>2</sub>/CS dispersion on a holey carbon grid followed by drying under ambient conditions. TEM imaging was conducted on a Philips CM-12 TEM at 80 kV using a Gatan model 791 CCD camera. Atomic force microscopy (AFM) imaging was conducted on a Bruker Multimode V system in ScanAsyst noncontact mode using ScanAsyst-Air tips (2 nm tip diameter). Processing of the AFM images was done using Gwyddion software package version 2.52. Raman spectra of the MoSe<sub>2</sub>/CS nanosheets and CS alone were obtained using a WITec alpha300R confocal Raman microscope system. The excitation laser wavelength was 532 nm, and the objective lens was 50× to prevent the solution from having direct contact with the lens. The total laser power was limited to 1 mW to prevent damage to the samples. X-ray diffraction (XRD) of MoSe<sub>2</sub>/CS nanosheets and CS alone was measured with a Rigaku MiniFlex Benchtop XRD with a 600 W anode X-ray diffractometer. Measurements of the Fourier transform infrared (FT-IR) spectra of MoSe<sub>2</sub>/CS nanosheets and CS alone were conducted using a PerkinElmer Spectrum GX. The thermal decomposition profiles of MoSe<sub>2</sub>/CS nanosheets, CS alone, and bulk MoSe<sub>2</sub> powder were obtained using a Setaram LABSYS EVO system under a nitrogen atmosphere and running between 10 to 700 °C using a heating rate of 10 °C/min. X-ray photoelectron spectroscopy (XPS) was conducted on a Thermo Scientific ESCALAB 250Xi, and the data was analyzed using CasaXPS.

**Fungal Cell Preparation.** Overnight cultures of *I. orientalis, S. cerevisiae,* and *C. parapsilosis* were grown in YM broth at 30 °C. *C. albicans, C. neoformans,* and *C. gattii* were grown in SDB medium at 30 °C for 16 h. *A. fumigatus, F. falciforme,* and *F. verticillioides* were grown in PDB medium at 26 °C for 48 h. Fungal cells were cultured to the midexponential growth phase with 0.4 optical density (OD) at 600 nm. Cells were centrifuged at 2500 rpm for 5 min, followed by washing of the pellets with 1× phosphate buffered saline (PBS). The final pellets were resuspended in their respective growth media, and OD $_{600}$  was measured. Cells were then diluted to  $10^7$  colony-forming units per milliliter (CFU ml $^{-1}$ ). All the experiments in this work involving fungal cells were repeated in triplicate.

Measurement of Minimum Fungicidal Concentration. Minimum fungicidal concentration (MFC) values for different fungal strains were determined using varying concentrations of MoSe<sub>2</sub>/CS. The fungal cell samples were diluted 100-fold in their respective growth media and allowed to grow until they reached OD<sub>600</sub> = 0.4 while shaking at 250 rpm. After washing and redispersion, fungal cultures were incubated with varying concentrations of MoSe<sub>2</sub>/CS ranging from 1.56 to 150  $\mu$ g ml<sup>-1</sup> for 3 h each. After the incubation step, the treated fungi were then deposited in in agar plates using the serial dilution method. The fungal cells then grew overnight before the surviving colonies were counted. All experiments were done in triplicate.

Measurement of Minimum Inhibitory Concentration. Minimum inhibitory concentrations (MIC) values were determined by treating the fungal strains with varying concentrations of MoSe<sub>2</sub>/CS, including the MFC value for each respective strain. One hundred microliters of the fungal cell culture at a concentration of  $10^5\,\mathrm{CFU}\,\mathrm{ml}^{-1}$  and  $100\,\mu\mathrm{L}$  of MoSe<sub>2</sub>/CS were incubated together at 30 °C in a 96-well plate in their respective growth media while shaking at 250 rpm. The OD values at 600 nm of each well in the plate were measured and recorded for 24 h at 30 min intervals using a BioTek Synergy Neo2 microplate spectrophotometer. Negative controls containing cells without MoSe<sub>2</sub>/CS were measured in parallel. OD measurements were plotted for each MoSe<sub>2</sub>/CS concentration to find the lowest value where the optical density stayed the same, indicating full inhibition of cell growth over time. This concentration is defined as the MIC. All experiments were performed in triplicate.

**Biocompatibility of MoSe<sub>2</sub>/CS.** The cytotoxicity of MoSe<sub>2</sub>/CS toward human embryonic kidney 293 cells (HEK293) cells was evaluated by alamarBlue and cell counting assays (CCK-8). The HEK293 cells were deposited in 96-well microplates with DMEM at a density of  $1 \times 10^5$  cells ml<sup>-1</sup> in a 200  $\mu$ L volume. The cells grew for 24 h at 37 °C in 5% CO<sub>2</sub>, followed by washing of the plates with DPBS. Then, the MoSe<sub>2</sub>/CS at different concentrations was incubated with the HEK293 cells for 3 h at 37 °C in 5% CO<sub>2</sub>, followed by washing of the wells three times with 1× DPBS to remove any cells that are not attached. The remaining attached cells were then incubated with 200  $\mu$ L of 10% (vol %) alamarBlue solution in DMEM at 37 °C in 5% CO<sub>2</sub> for 5 h to check their viability. The fluorescence intensity (FI 590) was measured at 530 nm (excitation) and 590 nm (emission) using a BioTek Synergy Neo2 microplate spectrophotometer. Cell damage was expressed as the fluorescence relative to that of DMEM alone as a control sample.

Similarly, XTT assays were also performed to check the biocompatibility of MoSe $_2$ /CS against HEK293 cells. A 10 vol % CCK-8 solution was introduced to the treated and washed mammalian cells to reach a 200  $\mu$ L total volume, followed by 2 h of incubation at 37 °C in 5% CO $_2$ . After incubation with the CCK-8 solution, 180  $\mu$ L of the supernatant was collected and deposited in a 96-well microplate so that the absorbance at 450 nm could be measured using a BioTek Synergy Neo2 microplate spectrophotometer. Control samples of HEK293 cells treated with just DMEM without any MoSe $_2$ /CS were also measured. The absorbance of DMEM was also measured and subtracted from all the above values. All the measurements were conducted in triplicate.

The percentage difference in reduction between treated and control cells in the alamarBlue cytotoxicity assay was calculated using the formula

% biocompatibility = 
$$\frac{\text{FI 590(treated sample)}}{\text{FI 590(control sample)}} \times 100$$
 (1)

where FI 590(treated sample) and FI 590(control sample) are the fluorescence intensity obtained at 590 nm emission and 530 nm excitation for the treated and control samples, respectively.

The percentage of viable cells in the cell counting proliferation assay was calculated using the formula

% cell viability = 
$$\frac{\text{abs(treated sample)}}{\text{abs(control sample)}} \times 100$$
 (2)

where abs(treated sample) and abs(control sample) are the absorbance at 450 nm of the treated and control samples, respectively.

**Hemolysis Assay.** Fresh single-donor human red blood cells (RBCs) were diluted to a ratio of 1:20 in PBS solution at a pH of 7.4, centrifuged to form a pellet (1000 rcf, 10 min), and washed in PBS three times. The RBCs were counted using a cell counter and diluted to  $2\times10^7$  cells ml $^{-1}$  as the final concentration. Equal volumes of RBCs were incubated in a 96-well plate for 3 h at 37  $^{\circ}$ C with varying concentrations of MoSe $_2$ /CS in a humidified atmosphere with 5% CO $_2$ . Subsequently, the 96-well plate was centrifuged (1000 rcf, 10 min), and 100  $\mu$ L of the supernatant was extracted and moved to a fresh black 96-well plate. The amount of hemoglobin released by the RBCs that undergo lysis was measured as the optical absorbance at 405 nm (abs) using a BioTek

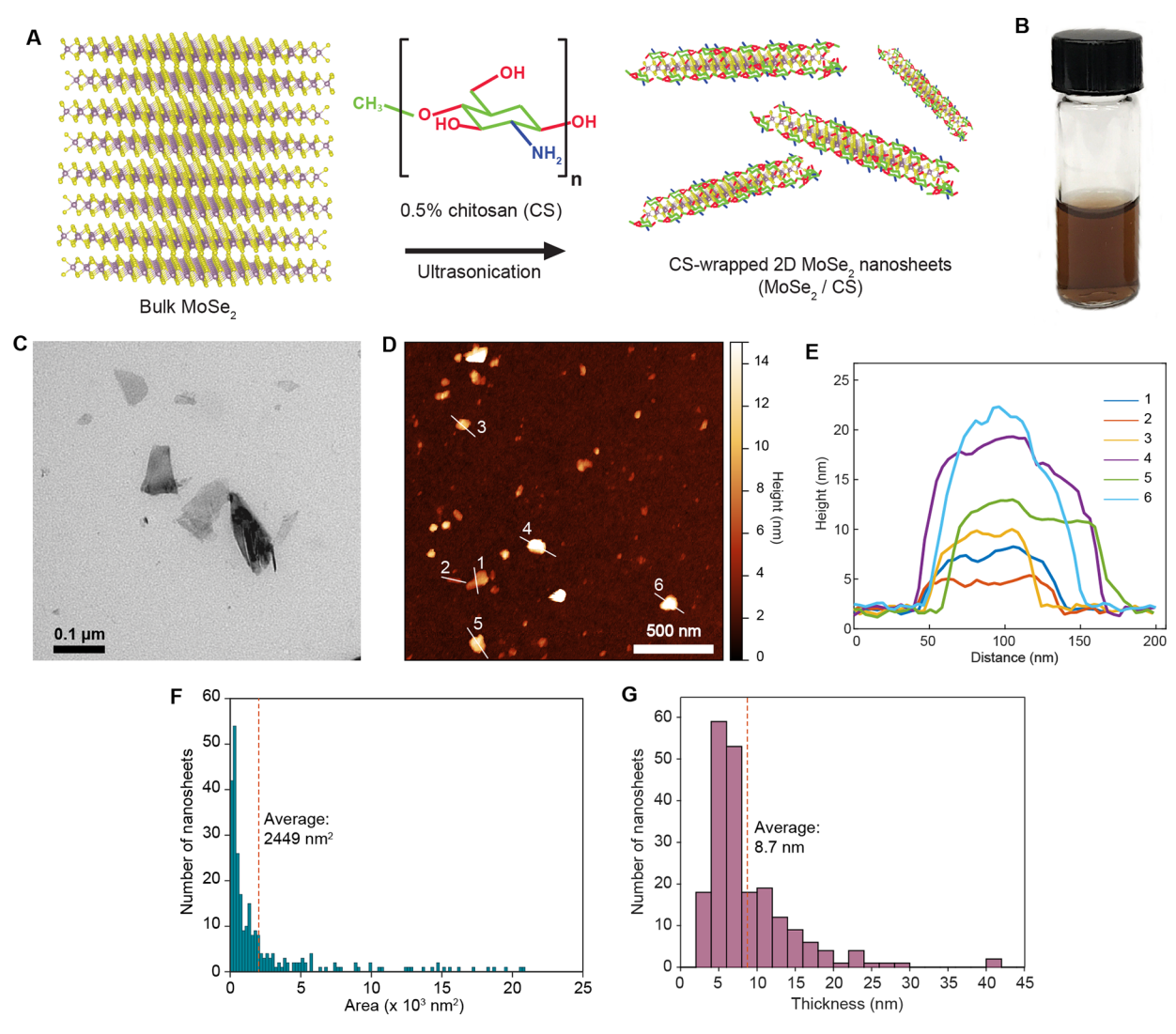


**Figure 1.** Preparation and characterization of MoSe<sub>2</sub>/CS nanosheets. (A) Schematic illustration of exfoliation of bulk MoSe<sub>2</sub> in 0.5% CS solution to form MoSe<sub>2</sub> nanosheets encapsulated in CS (MoSe<sub>2</sub>/CS). In the MoSe<sub>2</sub> structure, yellow spheres are Se atoms, and purple spheres are Mo atoms. (B) Glass vial containing a dark brown MoSe<sub>2</sub>/CS dispersion. (C) Representative transmission electron microscopy (TEM) image showing dispersed MoSe<sub>2</sub>/CS nanosheets used for measuring surface area distribution. (D) Representative atomic force microscopy (AFM) image showing dispersed MoSe<sub>2</sub>/CS nanosheets of varying thicknesses deposited on a substrate used for measuring thickness distribution. (E) Height profile of six different individual flakes marked in (D). (F) Surface area distribution of nanosheets from TEM images, with an average area of 2449 nm<sup>2</sup>. (G) Thickness distribution of MoSe<sub>2</sub>/CS nanosheets, with an average thickness of 8.7 nm.

Synergy Neo2 microplate spectrophotometer. RBCs treated by 1% Triton X-100 (1:1 vol/vol) were used as the positive control, while RBCs suspended in PBS were taken as the negative control. The percent hemolysis was plotted against the MoSe<sub>2</sub>/CS concentration, and the experiment was performed in triplicate.

The formula to calculate the percentage of hemolysis was

% hemolysis = 
$$\frac{abs(treated sample) - abs(negative control)}{abs(positive control) - abs(negative control)} \times 100$$
 (3)

Electron Microscopy of Fungal Cell Morphology. Fungal strains were treated with 75  $\mu$ g ml<sup>-1</sup> of MoSe<sub>2</sub>/CS followed by further treatment to prepare them for electron microscopy. For transmission electron microscopy (TEM) imaging, samples treated by MoSe<sub>2</sub>/CS and control samples were fixed in a suspension with 2.5% glutaraldehyde in Dulbecco's phosphate-buffered saline (DPBS) at 4 °C overnight followed by washing in DPBS. Cells were then placed into a drop of 1% agarose on a glass slide and treated with 1% osmium tetroxide (OsO<sub>4</sub>) in DPBS for 1 h, thoroughly washed with ultrapure water, and dehydrated in a graded acetone series (20, 40, 60, 80, and

100%). The samples were then infiltrated and embedded using Spurr's epoxy resin. Sections were then cut to 70 nm thickness using a Leica Ultracut-R microtome and then stained by uranyl acetate and lead citrate. The TEM microscope was a Philips CM-12 operating at 80 kV, and the camera was Gatan model 791 CCD. For scanning electron microscopy (SEM) imaging, the same fixing and washing procedure used for TEM samples was used. Washed cells were then concentrated into a small volume of DPBS and applied to poly-L-lysine (PLL)-coated coverslips. After 10 min, excess cells were removed by briefly rinsing in DPBS, and the coverslips were transferred to a solution of 1% OsO<sub>4</sub> in DPBS at room temperature for 1 h, followed by thorough washing with deionized water. Samples were dehydrated in a graded ethanol series (20, 40, 60, 75, 90, and 100%) and critical point dried in a Balzers-Union CPD-020 unit using carbon dioxide as the transition fluid. After routine mounting on aluminum stubs, the samples were coated with 10-12 nm of gold-palladium by sputtering in a Technics Hummer-II system. The SEM system was a JEOL JSM6300 with 15 kV acceleration voltage, and the digital processor for acquiring images was an IXRF model 500.

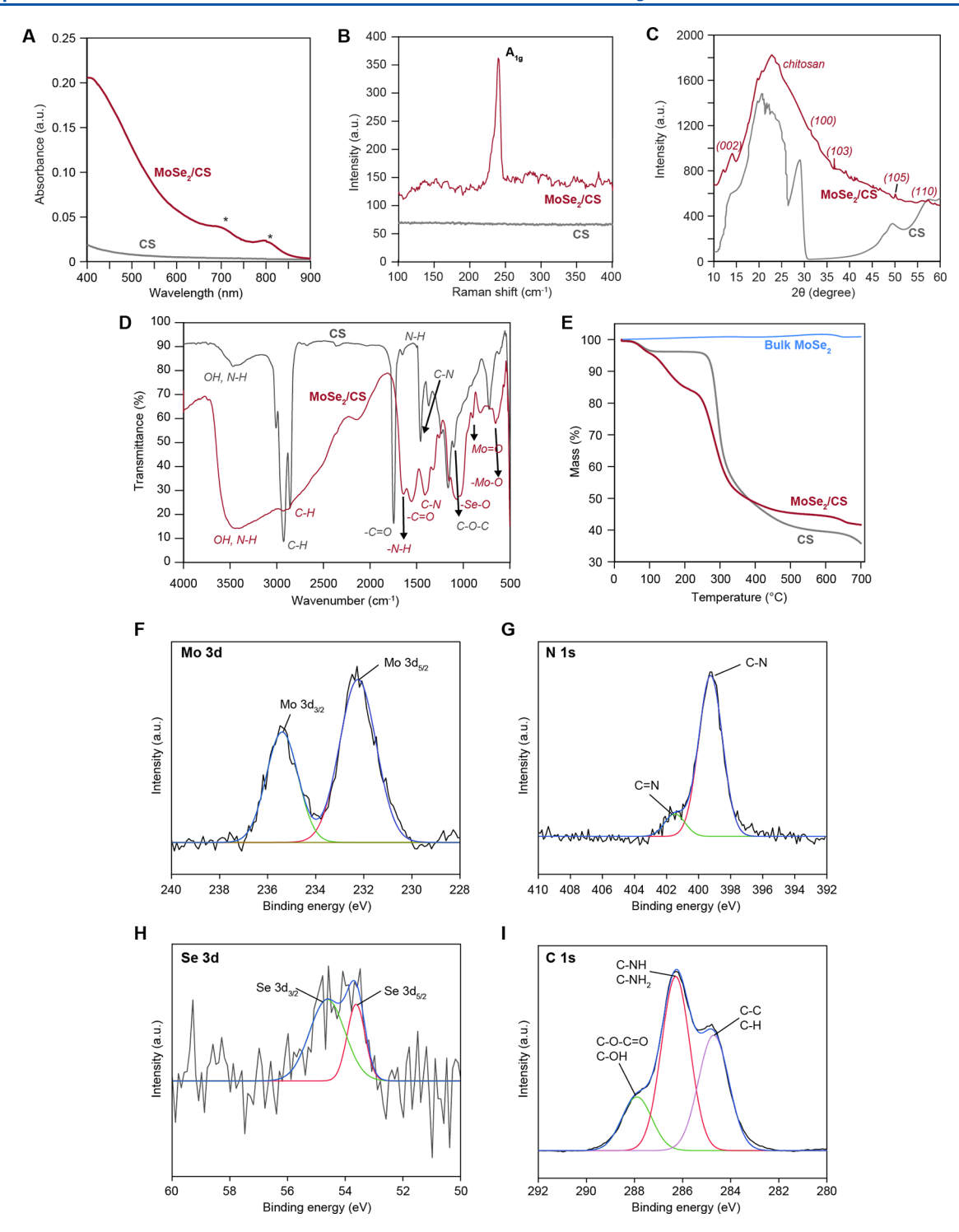


Figure 2. Chemical characterization of  $MoSe_2/CS$  nanosheets. (A) UV–Vis absorbance spectra of  $MoSe_2/CS$  nanosheets (red) and CS solution (gray). The  $MoSe_2$  characteristic excitonic peaks are marked by asterisks at ~700 and ~800 nm. (B) Raman spectra of  $MoSe_2/CS$  nanosheets (red) and CS solution (gray). The characteristic  $A_{1g}$  peak of  $MoSe_2$  is shown. (C) X-ray diffraction (XRD) pattern of  $MoSe_2/CS$  nanosheets (red) and CS (gray). Characteristic peaks are labeled. (D) Fourier transform infrared (FTIR) spectra of  $MoSe_2/CS$  nanosheets (red) and CS (gray). (E) Thermogravimetric analysis (TGA) curves of bulk  $MoSe_2$  (blue),  $MoSe_2/CS$  nanosheets (red), and CS (gray). (F–I) X-ray photoelectron spectroscopy (XPS) analysis of  $MoSe_2/CS$  nanosheets, showing high-resolution spectra in the (F) Mo3d region, (G) N1s region, (H) Se 3d region, and (I) C1s region.

**Confocal Scanning Laser Microscopy (CSLM).** For fungal cell visualization by CSLM, fungal cells of *C. albicans* (unicellular) and *A. fumigatus* (filamentous) were grown overnight and then diluted in SDB medium to  $3 \times 10^7$  CFU ml<sup>-1</sup> and transferred to four-well  $\mu$ -slides from ibidi. They were incubated with 0, 25, 50, and 100  $\mu$ g ml<sup>-1</sup> concentrations of MoSe<sub>2</sub>/CS for 3 h at 30 °C. Following the incubation

step, each sample was further incubated for 30–35 min at 30 °C in a fluorescent stain mixture containing 1  $\mu$ L ml<sup>-1</sup> of FUN-1 cell stain (Fun 1, excitation at 543 nm and emission at 560 nm) and 5  $\mu$ L ml<sup>-1</sup> solution of concavalin A–Alexa Fluor 488 conjugate (ConA, excitation at 488 nm and emission at 505 nm) in PBS. The stained cells were then imaged. In metabolically active cells, the FUN 1 dye is converted into

red-emitting intravacuolar structures so that live cells appear to have a red interior in CSLM images. The ConA fluorescent green dye binds to the glucose and mannose residues of cell walls so that cells appear to have a green exterior in CSLM images. The CSLM instrument was a Nikon C2 system mounted on a Zeiss Axiovert100 M microscope (Carl Zeiss, Inc.), and the excitation lasers were Ar and He lasers.

**Antifungal Mechanism Studies.** Evaluation of the antifungal mechanism of MoSe<sub>2</sub>/CS was determined using flow cytometric assays. For the analysis of membrane permeabilization, *C. albicans* was cultured overnight and then diluted in the SDB medium to  $3\times10^7$  CFU ml $^{-1}$ . Aliquots of the fungal suspension were incubated with 0, 25, 50, and 100  $\mu \mathrm{g}$  ml $^{-1}$  concentrations of MoSe<sub>2</sub>/CS nanosheets at 37 °C for 3 h. The fungal suspensions were then incubated at 37 °C in the dark for 60 min in a solution of bis-(1,3-dibutylbarbituric acid) trimethine oxonol (DiBAC<sub>4</sub>) at a final concentration of 1  $\mu \mathrm{M}$  to assess changes in the transmembrane potential.

Changes in membrane integrity due to treatment of fungi with MoSe<sub>2</sub>/CS were measured by incubating each fungal sample with a filtered solution of propidium iodide (PI) at a final concentration of 10  $\mu$ g ml<sup>-1</sup> at 37 °C for 60 min. The positive control was a suspension of fungal cells that were not treated by MoSe<sub>2</sub>/CS and then pelleted and suspended in absolute ethanol at  $-20~^{\circ}\text{C}$  for 30 min. The positive control sample was centrifuged at 1000g for 10 min, aspiration was used to remove the ethanol, and the resulting pellet was then suspended in SDB medium before adding PI dye in the same manner as described for the treated samples. To quantify the changes in membrane permeability due to MoSe<sub>2</sub>/CS, the fluorescence intensity of the cells was measured using a Stratedigm A600 HTAS cytometer with an argon laser as excitation source (488 nm, 5 mW). Green (525 nm) or red (610 nm) filtered light was detected using a photomultiplier tube fluorescence detector set to logarithmic amplification. An electronic gating threshold was set on the forward scattering detector to remove both optical and electronic noise. The flow rate of the system was limited to 200 events/s so that only one cell is measured at a time. A minimum of 20,000 detection events were acquired for each sample. All experiments described here were conducted in triplicate. The percentage of depolarized and disintegrated cells were calculated by comparing the number of events in the positive control sample to that in the treated and negative control samples.

The percentage of cytoplasmic protein leakage was analyzed using the Bradford assay. *C. albicans* was cultured overnight and then diluted in SDB medium to a concentration of  $3\times10^7$  CFU ml $^{-1}$ . Aliquots of the fungal suspension were extracted and incubated with 0, 25, 50, and 100  $\mu \rm g \ ml^{-1}$  concentrations of MoSe $_2$ /CS nanosheets at 37 °C for 3 h. After incubation, each sample was centrifuged at 5000g for 5 min. For each sample, 0.1 mg ml $^{-1}$  of Coomassie Brilliant Blue G-250 was added to the collected supernatant and allowed to incubate at room temperature for 10 min. Upon reaction with the leaked cytoplasmic protein, the color changes from red to blue. The absorbance at 595 nm was measured using a BioTek Synergy Neo2 microplate spectrophotometer. Calculations were done using 1% BSA as the positive control.

### RESULTS

#### Preparation and Characterization of 2D MoSe<sub>2</sub>/CS.

Chitosan (CS) is a naturally occurring linear polymer consisting of randomly ordered D-glucosamine and N-acetyl-D-glucosamine units. Acetyl moieties within the N-acetyl-D-glucosamine units provide a bulky group keeping the nanosheets from aggregating due to steric repulsion, whereas the amine groups (-NH<sub>2</sub>) in D-glucosamine act as a hydrophilic outer layer to interface with the surrounding aqueous solution. Bulk MoSe<sub>2</sub> powder was dispersed in 0.5% w/v low-molecular weight CS in 1% acetic acid using ultrasonication (Figure 1A) to form CS-wrapped MoSe<sub>2</sub> nanosheets. The MoSe<sub>2</sub>/CS dispersion appears dark brown (Figure 1B) and has a maximum concentration of ~0.32 mg ml<sup>-1</sup>. Transmission electron microscopy (TEM) images (Figure 1C) and atomic force microscopy (AFM) images (Figure 1D) showed the 2D nature of the dispersed

nanosheets, with some example height profiles shown in Figure 1E. The nanosheets produced by exfoliation in CS have a distribution of areas and thicknesses. We used TEM imaging to obtain a histogram of nanosheet areas (Figure 1F) and AFM imaging to obtain a histogram of nanosheet thicknesses (Figure 1G). Over 200 individual nanosheets were analyzed to obtain each histogram. The average area obtained from the TEM images was about 2449 nm². The vast majority of nanosheets were about 2-7 nm thick, corresponding to few-layered sheets, but could be as thick as  $\sim 40$  nm. The average thickness was about 8.7 nm.

The ultraviolet—visible light (UV—Vis) absorption spectrum in Figure 2A shows the characteristic excitonic peaks at  $\sim$ 700 and ~800 nm found in single- or few-layered 2D MoSe<sub>2</sub>; these peaks are not present in the spectrum from CS solution alone.<sup>45</sup> Raman spectroscopy of MoSe<sub>2</sub>/CS (Figure 2B) showed the characteristic A<sub>1g</sub> peak of MoSe<sub>2</sub> at ~241 cm<sup>-1</sup>, which is not present in the CS spectrum.<sup>58</sup> Next, X-ray diffraction (XRD) analysis shows further confirmation of exfoliated MoSe<sub>2</sub> nanosheets from bulk MoSe<sub>2</sub> (Figure 2C). For MoSe<sub>2</sub>/CS, we observe XRD peaks at ~14.08, 30.64, 36.6, 46.72, 50.1, and 56.06° corresponding to the (002), (100), (103), (105), and (110) planes of 2H-MoSe<sub>2</sub>. <sup>59,60</sup> Exfoliated nanosheets tend to have decreased XRD peak intensities and increased peak widths, as is observed here.<sup>38</sup> The broad feature between 20–25° for MoSe<sub>2</sub>/CS is attributed to the intense XRD peak seen in the same diffraction angle range for CS alone.<sup>38</sup> Thus, these measurements provide further evidence of the presence of CS.

The presence of chitosan was probed using Fourier transform infrared spectroscopy (FTIR) and thermogravimetric analysis (TGA) (see Figure 2D,E). The FTIR spectra of both  $MoSe_2/CS$ and CS (Figure 2D) clearly show several peaks in common: peaks around ~3600-3300 cm<sup>-1</sup> originating from -OH and -NH stretching, peaks around ~3000 to 2800 cm<sup>-1</sup> from −CH stretching, and peaks at  $\sim$ 1590 and  $\sim$ 1700 cm<sup>-1</sup> from the -C= O bond of the CS polymer. The slight shift in the -C=O peak may be due to polymer coating on top of the MoSe<sub>2</sub> nanosheets. Additionally, sharp peaks around ~1050 and 1200 cm<sup>-1</sup> due to stretching vibrations of -C—O—C bonds appear in the spectra of both MoSe<sub>2</sub>/CS and CS. <sup>45</sup> Finally, the MoSe<sub>2</sub>/CS spectrum shows peaks at  $\sim 1065$ ,  $\sim 927$ , and  $\sim 750$  cm<sup>-1</sup> due to the presence of -Se—O, Mo=O, and -Mo—O bonds, which are absent in the CS spectrum. 61 These particular peaks may indicate some degree of oxidation on the MoSe<sub>2</sub> surface and bonding with the CS structure. Thus, both the CS and MoSe<sub>2</sub>/ CS spectra have several peaks in common due to the CS structure, but in the MoSe<sub>2</sub>/CS spectrum alone, we have Moand Se-based peaks that correspond to surface interactions.

TGA curves of the MoSe<sub>2</sub>/CS nanosheets (Figure 2E) further supported the FTIR results. For bulk MoSe<sub>2</sub>, there was minimal weight loss across the measured temperature range, while the thermal decomposition profile of CS had a gradual loss in weight from 250 to 700 °C. For MoSe<sub>2</sub>/CS, the thermal degradation curve had a comparable shape to that of CS, which is consistent with the presence of CS. From the thermal mass loss, we calculate that ~94% of CS by weight was present in the sample. The decrease in weight occurring below 150 °C is likely due to the evaporation of the water content.<sup>62</sup>

X-ray photoelectron spectroscopy (XPS) was used to investigate the surface composition and bonding of the  $MoSe_2/CS$  nanosheets compared with CS alone. The spectrum of both  $MoSe_2/CS$  nanosheets and CS alone indicated the presence of Mo, Se, N 1s, C 1s, and O 1s (Figure 2F–I and

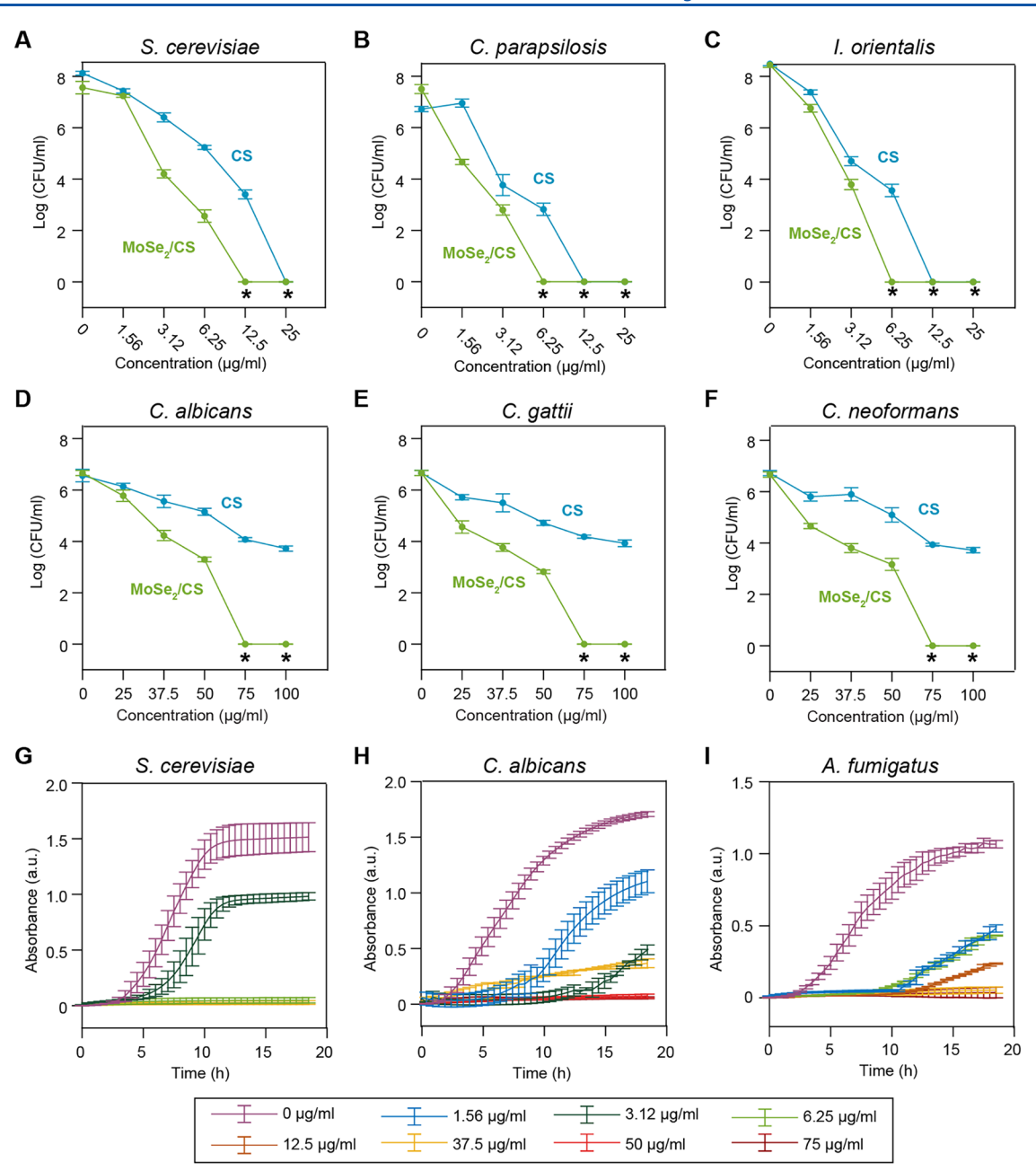


Figure 3. Antifungal activity of MoSe<sub>2</sub>/CS against unicellular and filamentous fungi. (A–C) The microdilution method was used to determine the minimum fungicidal concentration (MFC) values of BSL-1 fungi *S. cerevisiae* (A), *C. parapsilosis* (B), and *I. orientalis* (C), which were found to be 12.5, 6.25, and 6.25  $\mu$ g ml<sup>-1</sup>, respectively. (D–F) MFC values of BSL-2 fungi *C. albicans* (D), *C. gatti* (E), and *C. neoformans* (F) were determined to be 75  $\mu$ g ml<sup>-1</sup>. (G–I) Minimum inhibitory concentration (MIC) values were measured by optical absorbance over time for unicellular fungi *S. cerevisiae* (BSL-1) (G), *C. albicans* (BSL-2) (H), and filamentous *A. fumigatus* (BSL-2) (I) and were determined to be 3.125, 37.5, and 12.5  $\mu$ g ml<sup>-1</sup>, respectively. Asterisks indicate complete eradication of fungal cells at those concentrations.

Figure S1). The wide-scan spectra are shown in Figure S1. The high-resolution spectra for  $MoSe_2/CS$  nanosheets show Mo  $3d_{5/2}$  and Mo  $3d_{3/2}$  peaks (Figure 2F), N 1s peaks (Figure 2G), Se  $3d_{5/2}$  and Se  $3d_{3/2}$  peaks (Figure 2H), and C 1s peaks (Figure 2I). Corresponding spectra for CS alone (Figure S1) for C 1s, O 1s, and N 1s show similar features, verifying the presence of CS on the surface of  $MoSe_2$  nanosheets.

Antifungal Activity of MoSe<sub>2</sub>/CS. Fungi can be classified into two categories: (1) unicellular fungi, which includes S. cerevisiae, C. parapsilosis, I. orientalis, C. albicans, C. neoformans, and C. gattii; and (2) filamentous fungi, which include A. fumigatus. The minimum fungicidal concentration (MFC)

values of  $MoSe_2/CS$  were determined for both categories using the microdilution method (see the Experimental Section for more details) as shown in Figure 3. The MFC values of biosafety level 1 (BSL-1) strains *S. cerevisiae*, *C. parapsilosis*, and *I. orientalis* were determined to be 12.5, 6.25, and 6.25  $\mu$ g ml<sup>-1</sup>, respectively, of MoSe<sub>2</sub> dispersed in 5 mg ml<sup>-1</sup> of CS (Figure 3A—C and Table 1). The more resistant pathogenic BSL-2 fungi *C. albicans*, *C. gattii*, and *C. neoformans* required higher concentrations, with MFCs at 75  $\mu$ g ml<sup>-1</sup> (Figure 3D—F and Table 1).

The minimum inhibitory concentration (MIC) values for the unicellular fungi *S. cerevisiae*, *C. albicans*, and filamentous fungi *A*.

Table 1. MIC and MFC Values of MoSe<sub>2</sub>/CS against Different Fungal Strains

fungal strain	type	BSL level	incubation time (h)	$MFC \ (\mu g \ ml^{-1})$	$ MIC  (\mu g ml^{-1}) $
S. cerevisiae	unicellular	1	3	12.5	3.125
C. parapsilosis	unicellular	1	3	6.25	0.78
I. orientalis	unicellular	1	3	6.25	0.78
C. albicans	unicellular	2	3	75	37.5
C. neoformans	unicellular	2	3	75	1.56
C. gattii	unicellular	2	3	75	1.56
A. fumigatus	filamentous	2	3		12.5
F. verticillioides	filamentous	2	3		0.5
F. falciforme	filamentous	2	3		0.5

fumigatus were measured following the procedure described in the Experimental Section and were found to be 3.125, 37.5, and 12.5  $\mu$ g ml<sup>-1</sup>, respectively (Figure 3G–I). The microdilution test for MFC determination was not performed on *A. fumigatus* due to its filamentous nature and lack of individual colonies. The MICs of other strains including *C. parapsilosis, I. orientalis, C. neoformans, C. gattii, F. verticillioides,* and *F. falciforme* were determined to be 0.78, 0.78, 1.56, 1.56, 0.5, and 0.5  $\mu$ g ml<sup>-1</sup>, respectively (Figure S2 and Table 1).

The killing efficiency of MoSe<sub>2</sub>/CS was compared to 0.5% CS as a control. The 0.5% CS solution alone managed to kill only 95.75% of *S. cerevisiae*, 80.68% of *C. parapsilo*, and 79.0% of *I. orientalis* at similar applied concentrations of MoSe<sub>2</sub> (Figure 3A–C). On the other hand, in the case of BSL-2 fungi *C. albicans, C. gattii*, and *C. neoformans*, the 0.5% CS could only eliminate 58.6, 56.8, and 63.0% of these fungi strains, respectively (Figure 3D–F). Hence, we can conclude that 0.5% CS was far less potent against these strains and that the combined effect of MoSe<sub>2</sub> and CS results in the high killing efficiency of MoSe<sub>2</sub>/CS at lower concentrations.

**Biocompatibility of MoSe<sub>2</sub>/CS.** To test the effect of  $MoSe_2/CS$  on mammalian cells, we performed several biocompatibility assays (see the Experimental Section for more details). The hemolysis assay was performed by incubating human red blood cells (RBCs) with different concentrations of  $MoSe_2/CS$ . The same volume of 0.5% CS solution in separate

samples were used as controls (Figure 4A). After incubation for 3 h, only  $\sim$ 1.5 to 9% lysis of RBCs was observed for MoSe<sub>2</sub>/CS for concentrations as high as 150  $\mu g$  ml<sup>-1</sup> (marked by the red dashed line). Materials that induce up to 5% hemolysis of RBC (marked by the red dashed line in Figure 4A) are considered to be biocompatible. Therefore, we can conclude that MoSe<sub>2</sub>/CS can be considered as fairly biocompatible up to 150  $\mu g$  ml<sup>-1</sup>. Meanwhile, the 0.5% CS had a much stronger effect, causing lysis of  $\sim$ 7 to 50% when added at the same volumes as the MoSe<sub>2</sub>/CS preparations (Figure 4A). The surfactant Triton X is also used as a positive control for the complete lysis of RBCs.

The viability of human embryonic kidney cells (HEK 293) was tested using the XTT and alamarBlue viability assays with MoSe<sub>2</sub>/CS dispersions at different concentrations (Figure 4B,C). The colorimetric XTT assay results indicate that after incubation for 3 h with MoSe<sub>2</sub>/CS at concentrations from 0 to 75  $\mu$ g ml<sup>-1</sup>, more than 90% of cells were viable, which is considered to be biocompatible (marked by the red dashed line in Figure 4B,C). In fact, the MoSe<sub>2</sub>/CS nanosheets were more biocompatible than the CS alone. We also used the fluorescencebased alamarBlue assay. When treated by MoSe<sub>2</sub>/CS at all the concentrations we tested, the portion of viable cells is above  $\sim$ 90% (indicated by the red line) compared to the  $\sim$ 70–98% biocompatibility of 0.5% CS alone (Figure 4C). Hence, the abovementioned results all demonstrate the biocompatibility of MoSe<sub>2</sub>/CS at concentrations above the MFC level, and the XTT assay further shows that the viability of cells in 0.5% CS solution is actually lower than in MoSe<sub>2</sub>/CS at concentrations ranging from 37.5 to 100  $\mu$ g ml<sup>-1</sup>.

Confocal Scanning Laser Microscopy. Fluorescence imaging using confocal scanning laser microscopy (CSLM) was conducted on the unicellular fungi *C. albicans* and the filamentous fungi *A. fumigatus* to visualize the fungal cells and their viability after treatment with MoSe<sub>2</sub>/CS (Figure 5). The detailed sample preparation steps are described in the Experimental Section. In these CSLM images, intense green fluorescence results from the ConA dye binding to polysaccharides in the cell walls of the fungi, while the bright red fluorescence arises from the FUN 1 cell stain coming from the cytoplasm of metabolically active cells, where they form dense aggregates (red arrows). Cells that are metabolically inactive and likely dead are indicated by the absence of bright red aggregates

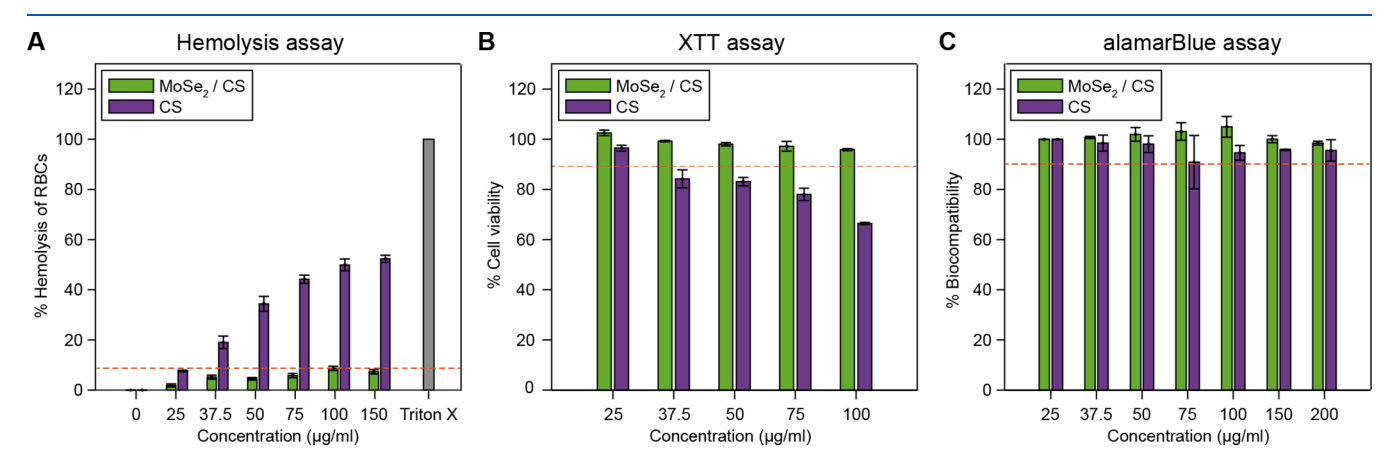


Figure 4. Biocompatibility test for  $MoSe_2/CS$  solution. (A) Hemolysis assay to determine the toxicity of  $MoSe_2/CS$  and 0.5% CS alone against RBCs. Percent hemolysis below the red dashed line (5% lysis) is considered nontoxic. (B) Percent cell viability of HEK293 cells when treated with different concentrations of  $MoSe_2/CS$  and 0.5% CS alone. Percent viability above the red dashed line at 90% is considered biocompatible. (C) Percent biocompatibility of HEK293 mammalian cells tested with the alamarBlue assay in the presence of  $MoSe_2/CS$  and 0.5% CS alone. Percent viability above the red dashed line at 90% is considered biocompatible.

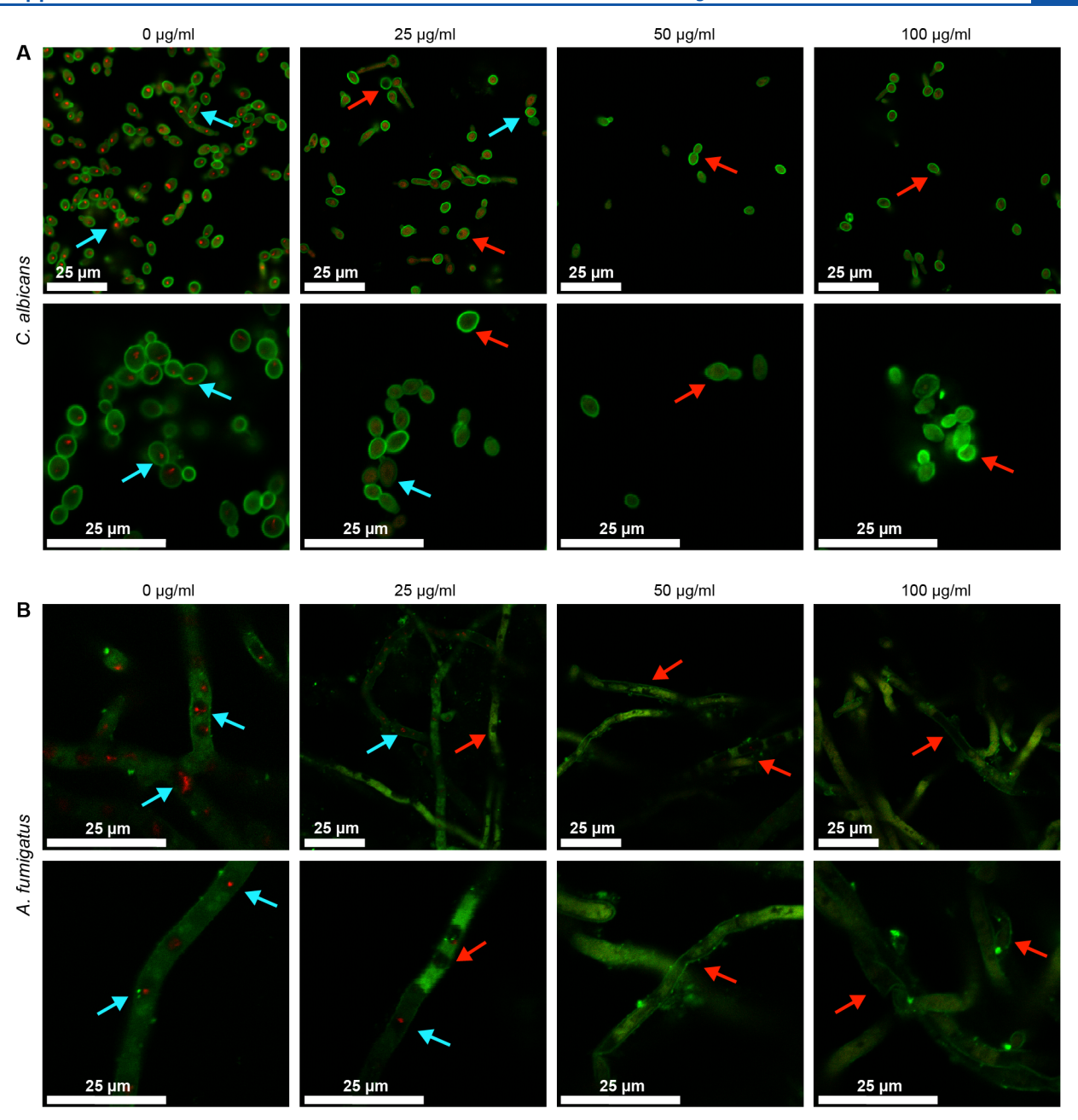


Figure 5. Fluorescence imaging of fungal cells by confocal scanning laser microscopy (CSLM). The structures appearing green (Con A stain) are the fungal cell walls and those appearing red (FUN 1 stain) are metabolically active cytoplasm. The viable cells are marked with cyan arrows. The absence of red aggregates in the cells signifies loss of viability or dead cells (red arrows). (A) *C. albicans* (unicellular) cells after treatment with MoSe<sub>2</sub>/CS at 0 (negative control), 25, 50, and 100  $\mu$ g ml<sup>-1</sup> for 3 h of incubation. The two rows of images are at different magnification levels. (B) *A. fumigatus* (filamentous) cells after treatment with MoSe<sub>2</sub>/CS at 0 (negative control), 25, 50, and 100  $\mu$ g ml<sup>-1</sup> for 3 h incubation.

(white arrows). Fungal cells were treated with MoSe<sub>2</sub>/CS at concentrations of 0 (negative control), 25, 50, and 100  $\mu g$  ml<sup>-1</sup> with 3 h incubation. A stark difference is observed between samples that were treated with 0  $\mu g$  ml<sup>-1</sup> and those treated with 50 and 100  $\mu g$  ml<sup>-1</sup> of MoSe<sub>2</sub>/CS. The negative control sample has substantially more red fluorescent aggregates, indicating many active cells, unlike samples treated with 25  $\mu g$  ml<sup>-1</sup> of MoSe<sub>2</sub>/CS, clearly indicating that there is some antifungal activity at that concentration. Samples treated with 50 and 100  $\mu g$  ml<sup>-1</sup> show close to no red fluorescence, indicating dead cells due to the MoSe<sub>2</sub>/CS treatment.

**Changes in Fungal Cell Morphology.** To observe changes in fungal cell morphology after treatment with MoSe<sub>2</sub>/CS at the

MFC, TEM and SEM imaging were performed on *C. albicans* and *A. fumigatus* (Figure 6). Cells were prepared for electron microscopy as described in the Experimental Section. Fungi treated with MoSe<sub>2</sub>/CS were compared to untreated control samples of fungi that were subjected to the same sample preparation conditions in the absence of MoSe<sub>2</sub>/CS. A stark difference was observed between the treated and untreated fungi. SEM imaging showed that the untreated *C. albicans* had intact unicellular cells and the untreated *A. fumigatus* had healthy filaments (Figure 6A,C). In contrast, the treated cells showed distinct membrane damage, breaking of filaments, and deformed cells (Figure 6B,D). The cross-sectional views in TEM images of the control samples reveal healthy cells with unbroken cell

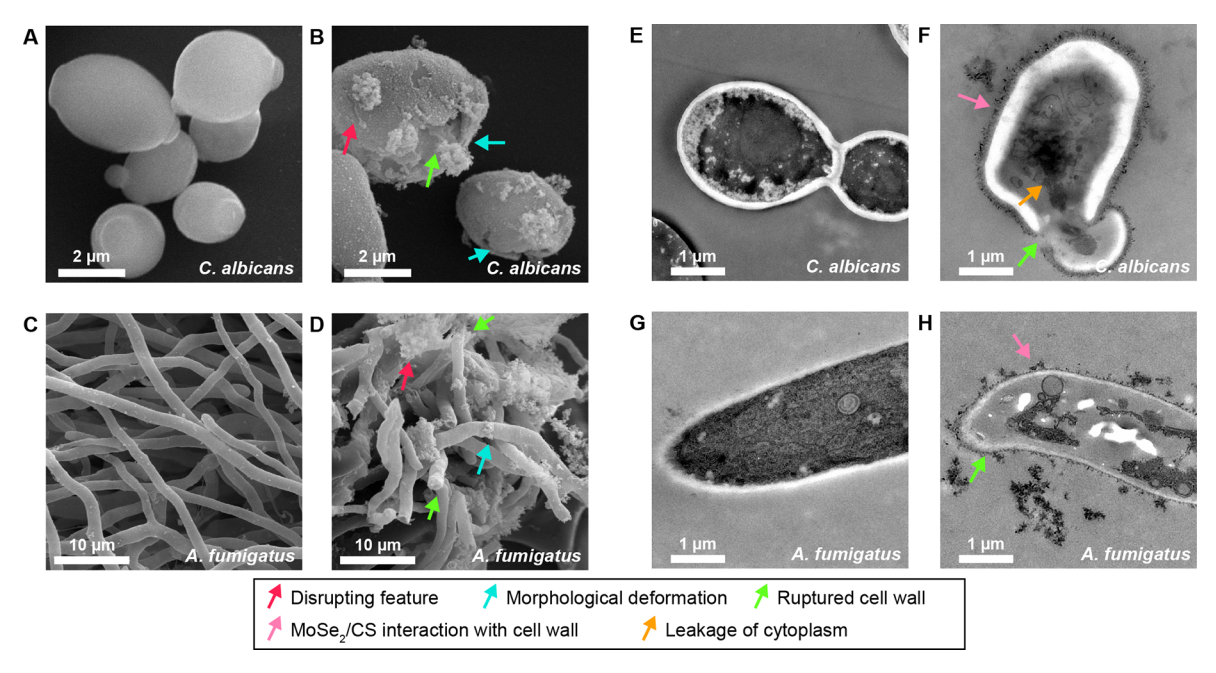


Figure 6. Morphology of cells and multimodal killing mechanism of MoSe<sub>2</sub>/CS against *C. albicans* and *A. fumigatus*. (A, C) SEM images of healthy control cells of *C. albicans* (A) and *A. fumigatus* (C). (B, D) SEM images showing the disruptive features (red arrows), morphological deformation (cyan arrows), and broken outer membrane (green arrows) of *C. albicans* (B) and *A. fumigatus* (D) in the presence of MoSe<sub>2</sub>/CS. (E, G) TEM images of control cells of *C. albicans* (E) and *A. fumigatus* (G) with intact cytoplasm. (F, H) TEM images of *C. albicans* (F) and *A. fumigatus* (H) in the presence of MoSe<sub>2</sub>/CS showing MoSe<sub>2</sub> flakes interacting with the cell wall (pink arrows), leading to the rupturing of the cell wall (green arrows) and cytoplasmic leakage (orange arrows).

membranes and intact cytoplasms (Figure 6E,G). The treated samples showed sharp-edged MoSe<sub>2</sub>/CS nanosheets assembling around the fungal cells and filaments, broken outer cell walls, and leaking of cytoplasm, leading to the deformation of cells (Figure 6F,H). These observations indicate that the positively charged MoSe<sub>2</sub>/CS complexes localize around the negative outer membranes due to electrostatic interactions. The presence of these complexes weakens the cell wall, destabilizing and reducing its rigidity, leading to disruption and membrane damage. The high turgor pressure inside the cell combined with these disturbances to the membrane enables the breaking of the cell wall and cytoplasmic leakage. Results from TEM and SEM images strongly support the membrane disintegration and physical damage of the fungal cells after treatment with MoSe<sub>2</sub>/ CS similar to previous studies.<sup>38,45</sup> In our previous work, we have also studied the dose-dependent effect (1× MBC and 0.5× MBC) of MoSe<sub>2</sub>/ssDNA in killing bacteria using TEM and SEM imaging. The resulting images showed no significant difference in types of morphological changes at various concentrations of the material. We expect a similar trend with MoSe<sub>2</sub>/CS in this work. These results indicate that MoSe<sub>2</sub>/CS weakens, damages, inhibits, and kills both unicellular and filamentous fungi.

Fungal Membrane Potential and Membrane Integrity. The influence of MoSe<sub>2</sub>/CS on fungal cell membranes was investigated by flow cytometry experiments to measure the transmembrane potential and membrane integrity of the fungi. Previous studies of other antifungal agents have shown that fungicidal effects occur by destabilizing the transmembrane potential, which then leads to the lipid bilayer being disrupted or damaged.<sup>30</sup> The molecular probe DiBAC<sub>4</sub> was used to investigate membrane potential because it preferentially enters cells whose membrane potential has collapsed to fluorescently label them. The amount of depolarization was indicated by the degree of fluorescence: the higher the fluorescence, the higher

the depolarization. Cell counts are shown as a function of the DiBAC<sub>4</sub> fluorescence in Figure 7A for the following conditions: a negative control (no MoSe<sub>2</sub>/CS), cells that have been treated with 50 and 100  $\mu$ g ml<sup>-1</sup> of MoSe<sub>2</sub>/CS, and a positive control (cold absolute ethanol). The calculated proportion of damaged and intact cells are shown in the bar plots in Figure 7C. The cells in the negative control sample having a DiBAC<sub>4</sub> fluorescence peak at ~1.4 were healthy cells with normal transmembrane potential. After incubation for 3 h with MoSe<sub>2</sub>/CS at concentrations of 25, 50, and 100  $\mu$ g ml<sup>-1</sup> and positive control (cold absolute ethanol), the percentages of depolarized cells are 83.7, 99, 98.8, and 98.6%, respectively.

Next, fungal membrane integrity for fungal cells treated by  $MoSe_2/CS$  nanosheets was investigated by introducing fungal cells to propidium iodide (PI), a dye that enters damaged cell membranes and binds to nucleic acids to emit a bright red fluorescence. *C. albicans* was treated with  $MoSe_2/CS$  nanosheets at concentrations of 25, 50, and 100  $\mu g$  ml<sup>-1</sup> and with positive control (cold absolute ethanol) for 3 h (Figure 7B). The higher the PI fluorescence, the higher the disintegration of the membrane. The calculated proportion of cells with damage to the membrane integrity were 76.1, 99, 99.2, and 98.7%, respectively, as shown in the bar plots in Figure 7D. Again, the negative control without any  $MoSe_2/CS$  has fully intact cells. This experiment clearly demonstrated that the  $MoSe_2/CS$  nanosheets damage the fungal cell membranes, leading to subsequent cytoplasmic leakage as investigated further below.

**Cytoplasmic Protein Leakage.** When the lipid bilayer of a fungal cell is physically disrupted, cytoplasmic leakage is expected. We used the Bradford assay<sup>65</sup> to assess proteins leaking from *C. albicans* cells treated with MoSe<sub>2</sub>/CS nanosheets due to membrane damage. The results shown in Figure 7E indicate that the protein leakage from fungal cells increases with increasing concentration of MoSe<sub>2</sub>/CS nanosheets and is much

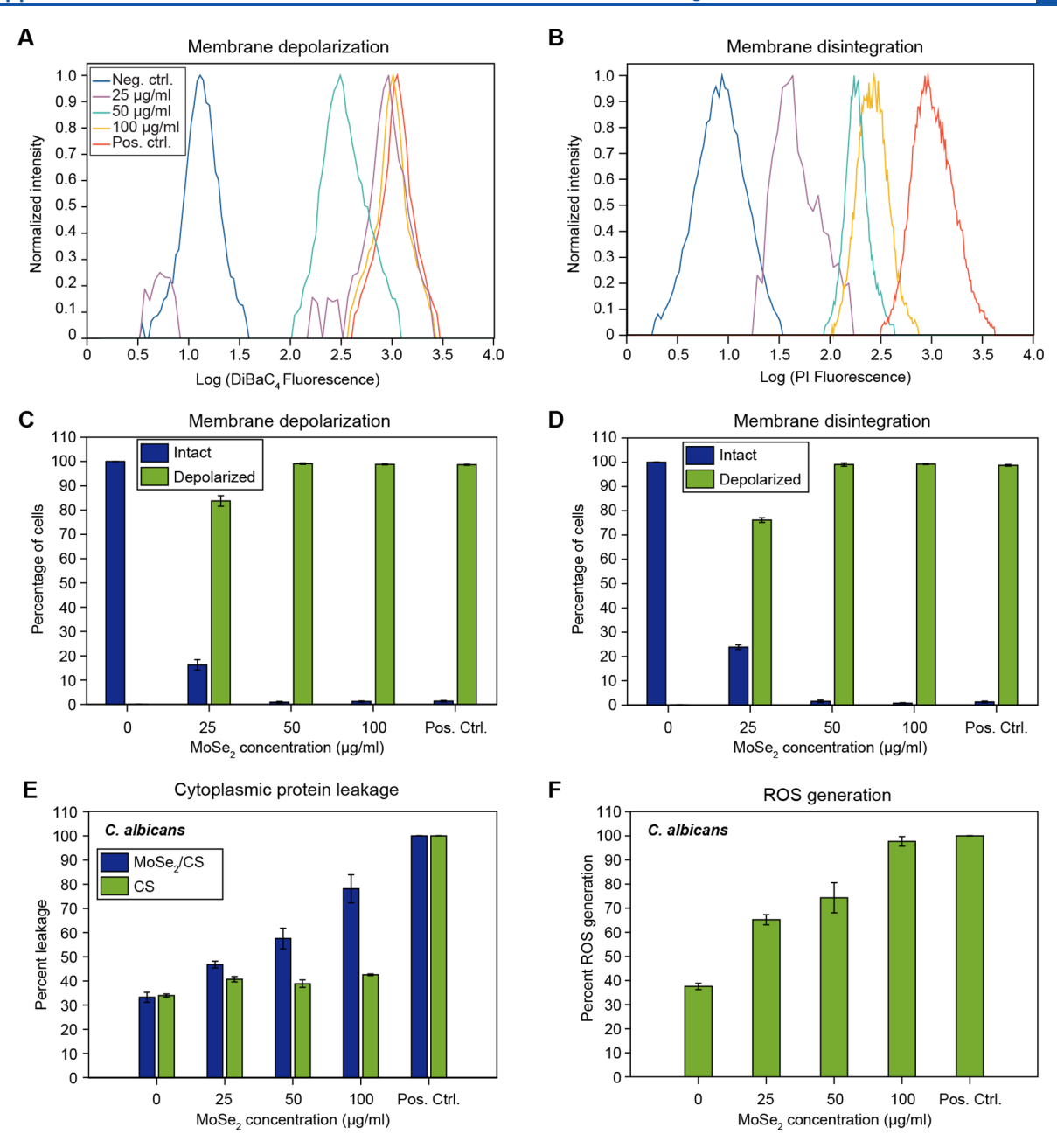


Figure 7. Mode of action of  $MoSe_2/Cs$  against *C. albicans*. (A) Plot of normalized event number in flow cytometry as a function of  $DiBAC_4$  (green) fluorescence intensity corresponding to the extent of depolarization of *C. albicans* cells upon treatment with negative control, 25, 50, and  $100 \,\mu g \, ml^{-1}$  of  $MoSe_2/CS$  and cold absolute ethanol (positive control) after 3 h incubation. (B) Plot of normalized event number in flow cytometry as a function of PI (red) fluorescence intensity showing the extent of depolarization of *C. albicans* cells upon treatment with negative control, 25, 50, and  $100 \,\mu g \, ml^{-1}$  of  $MoSe_2/CS$  and cold absolute ethanol (positive control) after 3 h incubation. (C) Bar plots of the proportion of cells with depolarization for the samples shown in panel (A). (D) Bar plots of the proportion of disintegrated cells for the samples shown in panel (C). (E) Percentage leakage of cytoplasm from *C. albicans* after 3 h treatment of with  $MoSe_2/CS$  nanosheets at different concentrations and compared with CS solution with 1% BSA as a positive control. (F) Bar plot showing the generation of reactive oxygen species (ROS) as a function of concentration of  $MoSe_2/CS$  with  $0.1\% \, H_2O_2$  as a positive control after 3 h of incubation.

higher than the leakage when the cells are treated with CS solution alone. Protein leakage was observed to be around 77.9% for MoSe<sub>2</sub>/CS nanosheets at 100  $\mu$ g ml<sup>-1</sup> compared to just 42.7% for CS solution alone. The leakage for the positive control, 1% bovine serum albumin (BSA), was 100%.

Reactive Oxygen Species (ROS) Generation. Previous studies in the literature have suggested that the antifungal activity of many nanomaterials involves intracellular oxidative stress due to the formation of reactive oxygen species (ROS) that can cause oxidative damage to proteins and nucleic acids in

cells.<sup>66</sup> In order to determine whether the membrane damage caused by MoSe<sub>2</sub>/CS nanosheets also leads to oxidative stress, we used the CellROX green reagent assay<sup>45,66</sup> to quantify the levels of intracellular ROS in fungal cells that have been treated with MoSe<sub>2</sub>/CS and compare them to cells that are untreated. We observed that treatment of *C. albicans* with MoSe<sub>2</sub>/CS nanosheets produced substantial intracellular ROS that increased with increasing nanosheet concentration (Figure 7F). At MoSe<sub>2</sub>/CS concentrations of 25, 50, and 100  $\mu$ g ml<sup>-1</sup>, ROS generation was 65.1, 75.3, and 97.7%, respectively, of the

value from the positive control (0.1%  $\rm H_2O_2$  solution). This result is in accordance with the membrane disintegration and cytoplasmic leakage showing a correlation between membrane damage and intracellular oxidative stress, which contribute to the antifungal efficacy of  $\rm MoSe_2/CS$ .

Treatment of C. auris. C. auris is a newly emerging pathogenic fungus that is resistant to multiple antifungal drugs and persists particularly in healthcare settings. In this study, MoSe<sub>2</sub>/CS was used to treat nine different strains from the C. auris panel identified by the CDC with the most resistance against all three classes of antifungal drugs. The MFC of  $MoSe_2/$ CS was determined using the microdilution method against three different C. auris isolates (0386, 0388, and 0389), C. duobushaemulonii (0394), C. haemulonii (0395), K. ohmeri (0396), C. krusei (0397), C. lusitaniae (0398), and S. cerevisiae (0399). The MFCs of the C. auris strains and C. krusei were all found to be between 100 and 150  $\mu g$  ml<sup>-1</sup>, as shown in Figure 8A-D and summarized in Table 2. The MFC for more susceptible isolates C. duobushaemulonii, C. haemulonii, K. ohmeri, C. lusitaniae, and S. cerevisiae were determined to be between 25 and 50  $\mu$ g ml<sup>-1</sup>, respectively, as shown in Figure S7 and summarized in Table 2. MIC measurements for C. auris (0389) and C. krusei strains revealed that they were inhibited at 50 and 25  $\mu$ g ml<sup>-1</sup>, respectively (Figure 8E,F). Each experiment was done in triplicate and compared with 0.5% CS in the absence of MoSe<sub>2</sub>. The results show excellent efficacy of MoSe<sub>2</sub>/ CS against all the isolates.

### DISCUSSION

In this study, we prepared MoSe<sub>2</sub> nanosheets encapsulated in chitosan that completely eradicated (i.e., 100% killing) both unicellular and filamentous fungi within 3 h of incubation at a various range of concentrations. Our results show superior performance in terms of MFC and MIC values and a short incubation duration compared to previous reports of various nanomaterials and nanoparticles acting as antifungal agents (see Table S2 for comparisons). Antifungal studies with carbonbased nanomaterials like SWCNTs after incubation for 3 h showed killing efficiency up to ~96% at a concentration of 500 μg ml<sup>-1</sup> against Fusarium graminearum and Fusarium poae. In comparison, our MoSe<sub>2</sub>/CS nanosheets against C. albicans had an MFC value of 75  $\mu$ g ml<sup>-1</sup> over the same incubation time.<sup>31</sup> Reduced graphene oxide (rGO) manages to inhibit (MIC) only 50% of Aspergillus niger after 7 days of incubation at 50 µg  $ml^{-1.48}$  In comparison, our MoSe<sub>2</sub>/CS inhibited the growth of A. fumigatus at a far lower concentration of 12.5  $\mu$ g ml<sup>-1</sup>. GO coupled with other nanomaterials like silver nanoparticles (AgNPs) shows increased inhibition in terms of MIC against C. albicans at 8  $\mu$ g ml<sup>-1</sup> but only after a far longer incubation period of 18 h. Low-molecular weight CS (LMWCS) has shown good antifungal efficiency against C. albicans with an MIC of <40  $\mu$ g ml<sup>-1</sup>, which is similar to the MoSe<sub>2</sub>/CS MIC of 37.5  $\mu$ g ml<sup>-1</sup>. However, the incubation period for LMWCS was considerably longer at 24 h instead of 3 h for our work. 52 The antifungal activity of another TMDC material, MoS2, has also been reported previously but only when modified with both CS and AgNPs (MoS<sub>2</sub>-CS-Ag), making it highly effective at just 6.8  $\mu$ g ml<sup>-1</sup> against Saccharomyces uvarum and 4.2 µg ml<sup>-1</sup> against Aspergillus niger. However, both these organisms were less virulent BSL-1 strains and were incubated for 72 h, 36 which is a far longer duration than our 3 h incubation time. Another study showed that a synthetic polymer for potential use in medical

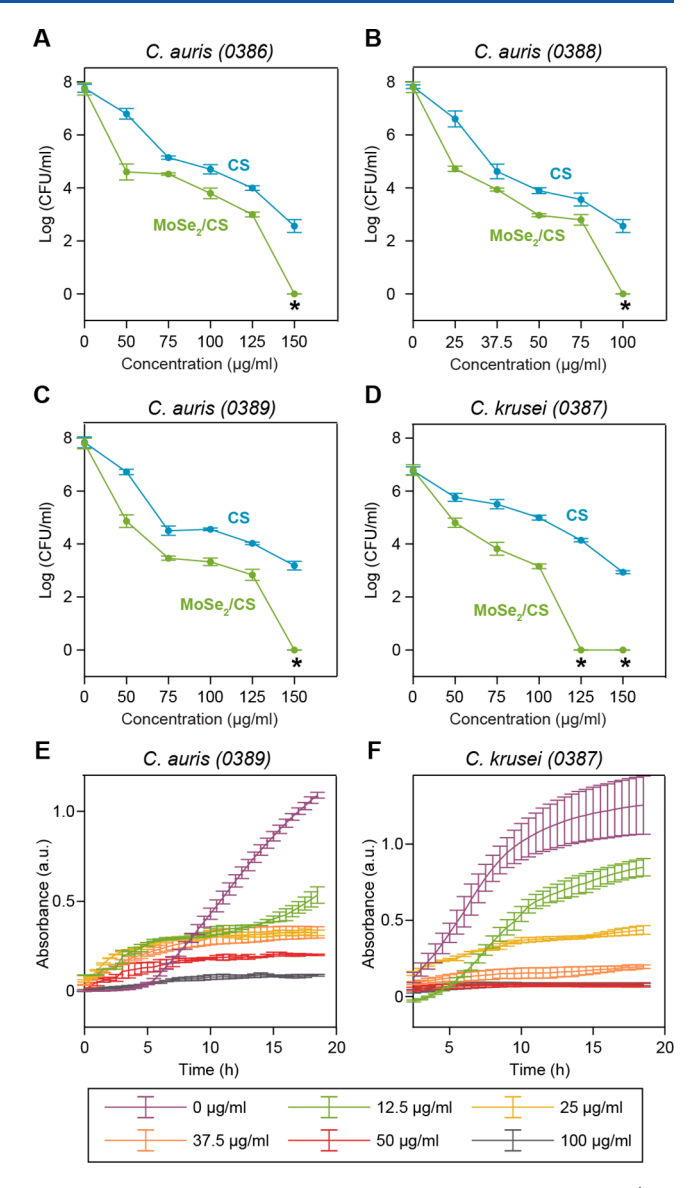


**Figure 8.** Antifungal activity of  $MoSe_2/CS$  against a *C. auris* panel. (A–D) CFUs at different concentrations to determine the MFC values of a BSL-2 *C. auris* panel including *C. auris* (0386), *C. auris* (0388), *C. auris* (0389), and *C. krusei* (0387), which were found to be 150, 100, 150, and 125  $\mu$ g ml<sup>-1</sup>, respectively, using the microdilution method. (E–F) Absorbance measured over time to determine MICs of *C. auris* (0389) and *C. krusei* (0387) (BSL-2), which were found to be 50 and 25  $\mu$ g ml<sup>-1</sup>, respectively. Asterisks indicate complete eradication of fungal cells at those concentrations.

devices had antimicrobial properties against several organisms but was ineffective when treating *C. auris.*<sup>67</sup>

Overall, the MoSe<sub>2</sub>/CS nanosheets here were tested against a wide range of fungal strains from BSL-1 to BSL-2 and demonstrated the capacity to completely eradicate them at varying concentrations. With MoSe<sub>2</sub>/CS, we observe complete eradication of various strains in the *C. auris* panel. In addition, there seems to be a correlation between the susceptibility of these *C. auris* isolates toward conventional antifungal drugs and toward MoSe<sub>2</sub>/CS. The isolates that exhibit higher MIC values when treated by known drugs like amphotericin B, fluconazole, and flucytosine (i.e., *C. auris* (0389)) also exhibited higher MFC when treated by MoSe<sub>2</sub>/CS, whereas *C. duobushaemulonii* or *C. haemulonii* with lower MIC values were more susceptible toward

Table 2. MIC and MFC Values of MoSe<sub>2</sub>/CS against Different Fungal Strains of C. auris

fungal strain	type	biosafety level	incubation time (h)	MFC ( $\mu$ g ml <sup>-1</sup> )	$MIC (\mu g ml^{-1})$
C. auris (0386)	unicellular	2	3	150	
C. auris (0388)	unicellular	2	3	100	
C. auris (0389)	unicellular	2	3	150	50
C. krusei (0397)	unicellular	2	3	125	25
C. duobushaemulonii (0394)	unicellular	2	3	50	
C. haemulonii (0395)	unicellular	2	3	37.5	
K. ohmeri (0396)	unicellular	2	3	37.5	
C. lusitaniae (0398)	unicellular	2	3	37.5	
S. cerevisiae (0399)	unicellular	2	3	37.5	

MoSe<sub>2</sub>/CS in the panel (Table S2). *C. auris* also showed higher MFC and MIC as compared to the *C. albicans* we tested before. Hence, MoSe<sub>2</sub>/CS was proven efficient against a panel of drugresistant fungal strains, making them a potent antifungal agent for potential use in healthcare settings.

To understand how MoSe<sub>2</sub>/CS inactivates fungal cells, we evaluated the transmembrane potential and membrane integrity of C. albicans under treatment with the nanosheets. MoSe<sub>2</sub>/CS successfully depolarized 99.9% of cells at a concentration of only 50  $\mu$ g ml<sup>-1</sup>. Even the cold absolute ethanol (positive control) was only able to depolarize 80.0% of the cells (Figure 7C). A previous study on C. albicans to examine depolarization effects due to carbon nanotubes functionalized with amphotericin B (fCNTs-AMB)<sup>30</sup> showed that effective depolarization was achieved by incubating for a much longer period of 16 h at 10  $\mu$ g ml<sup>-1</sup> concentration, with a depolarization of 92.7% of cells. Similarly, the extent of membrane damage after 3 h of incubation is significant, as shown by the shift in MoSe<sub>2</sub>/CS-treated cells compared to the control cells. The fast rate of damage within 3 h of incubation with *C. albicans* with MoSe<sub>2</sub>/CS shows a very high level of membrane damage, with 99.4 and 99.1% of cells disintegrated for 50 and 100  $\mu$ g ml<sup>-1</sup> of MoSe<sub>2</sub>/CS, respectively (Figure 7D). In a previous work with carbon nanotubes, 10  $\mu$ g ml<sup>-1</sup> of fCNTs-AMB incubated with *C. albicans* for 16 h led to membrane damage in 80% of cells. MoSe<sub>2</sub>/CS acts even faster than lytic antimicrobial peptides<sup>20</sup> with a shorter exposure time of 3 h, revealing evident depolarization and permeabilization effects. Such rapid depolarization with MoSe<sub>2</sub>/CS-treated cells is likely due to the electrostatic interaction of the cationic CS polymer with the negatively charged chitin on the fungal cell surface.

Other recent work in the literature on how bacterial membranes interact with other types of 2D nanosheets can offer insights into our MoSe<sub>2</sub>/CS system. In previous studies of the antibacterial activity of MoS2 nanosheets, they were shown to first attach onto the outer surface of the cell membranes of bacteria, form indentations in the membrane, and then insert themselves into the cells.<sup>68</sup> For CS-dispersed MoS<sub>2</sub> nanosheets against bacteria, the positively charged CS attached electrostatically to the surface of bacterial cells, which allowed the MoS<sub>2</sub> nanosheets to be embedded into the membrane via the formation of dents.<sup>38</sup> For fungi exposed to our MoSe<sub>2</sub>/CS system, the strong electrostatic interaction between MoSe<sub>2</sub>/CS nanosheets and the combination of polyglucan and chitin molecules in the fungal membrane initiates the antifungal activity. This CS-driven interaction helps the thin 2D MoSe<sub>2</sub> nanosheets puncture the cell membrane, which in turn destabilizes the turgor pressure of the cell so that the cytoplasm leaks out.<sup>68</sup> This synergistic effect quickly leads to the depolarization of the cell membrane, followed by changes in

membrane permeability and then leading to the disintegration of the cell membrane.

### CONCLUSIONS

MoSe<sub>2</sub> nanosheets dispersed in chitosan (MoSe<sub>2</sub>/CS) were prepared by liquid phase exfoliation from bulk MoSe2, resulting in a distribution of areas and thicknesses of nanosheets wrapped in CS as shown by TEM and AFM imaging. Treatment of a range of unicellular and filamentous fungi by the MoSe<sub>2</sub>/CS nanosheets revealed exceptional antifungal activity, with complete eradication with only a brief 3 h incubation period. The MFC concentrations of MoSe<sub>2</sub>/CS required to eradicate both unicellular and filamentous fungi ranged from 6.25 to 75  $\mu$ g ml<sup>-1</sup> of MoSe<sub>2</sub> dispersed in 5 mg ml<sup>-1</sup> of CS. The concentrations at which these different strains were inhibited were between 0.5 and 37.5  $\mu$ g ml<sup>-1</sup> of MoSe<sub>2</sub> in 5 mg ml<sup>-1</sup> of CS. Experiments with fluorescent probes were undertaken to determine the likely mechanisms of antifungal action. The MoSe<sub>2</sub>/CS nanosheets likely cause the death of fungal cells by membrane damage, membrane depolarization, metabolic inactivation, and cytoplasmic leakage. They were also highly potent against a panel of MDR C. auris fungi at concentrations ranging from 37.5 to 150  $\mu$ g ml<sup>-1</sup> within 3 h incubation time. Unlike other nanomaterialbased antifungal agents in the literature, the MoSe<sub>2</sub>/CS nanosheets in the current study are highly effective on their own and do not require more complex modifications as well as external nIR-assisted photothermal action. Aside from their exceptional antifungal activity, the MoSe<sub>2</sub>/CS nanosheets were also highly biocompatible toward mammalian cells. The remarkable antifungal performance of the MoSe<sub>2</sub>/CS nanosheets suggests that they are a promising new antifungal agent with potential uses in a variety of biomedical applications, which are particularly important given the threat of fungal pathogens.

### ASSOCIATED CONTENT

## Supporting Information

The Supporting Information is available free of charge at https://pubs.acs.org/doi/10.1021/acsanm.1c01013.

Additional XPS spectra; antifungal data; SEM images; TEM images; CSLM images; comparisons of antifungal activity with other drugs and nanomaterials (PDF)

### AUTHOR INFORMATION

#### **Corresponding Authors**

Qing Hua Wang — Materials Science and Engineering, School for Engineering of Matter, Transport and Energy, Arizona State University, Tempe, Arizona 85287, United States;
occid.org/0000-0002-7982-7275; Email: qhwang@asu.edu

Alexander A. Green — Biodesign Center for Molecular Design and Biomimetics, The Biodesign Institute and School of Molecular Sciences, Arizona State University, Tempe, Arizona 85287, United States; Department of Biomedical Engineering, Boston University, Boston, Massachusetts 02215, United States; Occid.org/0000-0003-2058-1204;

Email: aagreen@bu.edu

#### **Authors**

Sanchari Saha — Biodesign Center for Molecular Design and Biomimetics, The Biodesign Institute and School of Molecular Sciences, Arizona State University, Tempe, Arizona 85287, United States

Matthew S. Gilliam — Biodesign Center for Molecular Design and Biomimetics, The Biodesign Institute and School of Molecular Sciences, Arizona State University, Tempe, Arizona 85287, United States

Complete contact information is available at: https://pubs.acs.org/10.1021/acsanm.1c01013

#### Notes

The authors declare no competing financial interest.

#### ACKNOWLEDGMENTS

We acknowledge the use of facilities at the Life Science Electron Microscopy Lab at Arizona State University (ASU), Trevor Martin at the Metals Environmental and Terrestrial Analytical Laboratory at ASU for assistance with ICP-MS measurements, Yuqi Guo for assistance with AFM imaging, and the use of instruments at the Advance Light Microscopy Core facilities at the Biodesign Institute at ASU. We also acknowledge the CDC & FDA Antibiotic Resistant Isolate Bank, Atlanta (GA), for providing the *Candida auris* panel. Q.H.W., M.S.G., and A.A.G. acknowledge funding from NSF grant DMR-1610153. Q.H.W. acknowledges funding from DMR-1906030.

### REFERENCES

- (1) Lee, Y.; Puumala, E.; Robbins, N.; Cowen, L. E. Antifungal Drug Resistance: Molecular Mechanisms in *Candida albicans* and Beyond. *Chem. Rev.* **2021**, *121*, 3390–3411.
- (2) Armstrong-James, D.; Meintjes, G.; Brown, G. D. A Neglected Epidemic: Fungal Infections in HIV/AIDS. *Trends Microbiol.* **2014**, *22*, 120–127.
- (3) Cowen, L. E.; Sanglard, D.; Howard, S. J.; Rogers, P. D.; Perlin, D. S. Mechanisms of Antifungal Drug Resistance. *Cold Spring Harbor Perspect. Med.* **2015**, *5*, No. a019752.
- (4) Brown, G. D.; Denning, D. W.; Gow, N. A.; Levitz, S. M.; Netea, M. G.; White, T. C. Hidden Killers: Human Fungal Infections. *Sci. Transl. Med.* **2012**, *4*, 165rv13.
- (5) Bongomin, F.; Gago, S.; Oladele, R. O.; Denning, D. W. Global and Multi-National Prevalence of Fungal Diseases—Estimate Precision. *J. Fungi* **2017**, *3*, 57.
- (6) Savary, S.; Ficke, A.; Aubertot, J.-N.; Hollier, C. Crop Losses Due to Diseases and Their Implications for Global Food Production Losses and Food Security. *Food Secur.* **2012**, *4*, 519–537.
- (7) Casadevall, A. Don't Forget the Fungi When Considering Global Catastrophic Biorisks. *Health Secur.* **2017**, *15*, 341–342.
- (8) Fisher, M. C.; Henk, D. A.; Briggs, C. J.; Brownstein, J. S.; Madoff, L. C.; McCraw, S. L.; Gurr, S. J. Emerging Fungal Threats to Animal, Plant and Ecosystem Health. *Nature* **2012**, *484*, 186–194.
- (9) Garcia-Solache, M. A.; Casadevall, A. Global Warming Will Bring New Fungal Diseases for Mammals. *MBio* **2010**, *1*, No. e00061.
- (10) Jeffery-Smith, A.; Taori, S. K.; Schelenz, S.; Jeffery, K.; Johnson, E. M.; Borman, A.; Manuel, R.; Brown, C. S. *Candida auris*: A Review of the Literature. *Clin. Microbiol. Rev.* **2018**, *31*, No. e00029–17.

- (11) Satoh, K.; Makimura, K.; Hasumi, Y.; Nishiyama, Y.; Uchida, K.; Yamaguchi, H. *Candida auris* Sp. Nov., a Novel Ascomycetous Yeast Isolated from the External Ear Canal of an Inpatient in a Japanese Hospital. *Microbiol. Immunol.* **2009**, *53*, 41–44.
- (12) Rhodes, J.; Fisher, M. C. Global Epidemiology of Emerging Candida auris. Curr. Opin. Microbiol. 2019, 52, 84–89.
- (13) Schelenz, S.; Hagen, F.; Rhodes, J. L.; Abdolrasouli, A.; Chowdhary, A.; Hall, A.; Ryan, L.; Shackleton, J.; Trimlett, R.; Meis, J. F.; Armstrong-James, D.; Fisher, M. C. First Hospital Outbreak of the Globally Emerging *Candida auris* in a European Hospital. *Antimicrob. Resist. Infect. Control* **2016**, *5*, 35.
- (14) Spivak, E. S.; Hanson, K. E. Candida auris: An Emerging Fungal Pathogen. J. Clin. Microbiol. 2018, 56.
- (15) Chowdhary, A.; Kumar, V. A.; Sharma, C.; Prakash, A.; Agarwal, K.; Babu, R.; Dinesh, K.; Karim, S.; Singh, S.; Hagen, F. Multidrug-Resistant Endemic Clonal Strain of *Candida auris* in India. *Eur. J. Clin. Microbiol. Infect. Dis.* **2014**, *33*, 919–926.
- (16) Coelho, C.; Casadevall, A. Cryptococcal Therapies and Drug Targets: The Old, the New and the Promising. *Cell. Microbiol.* **2016**, *18*, 792–799.
- (17) Lockhart, S. R.; Etienne, K. A.; Vallabhaneni, S.; Farooqi, J.; Chowdhary, A.; Govender, N. P.; Colombo, A. L.; Calvo, B.; Cuomo, C. A.; Desjardins, C. A.; Berkow, E. L.; Castanheira, M.; Magobo, R. E.; Jabeen, K.; Asghar, R. J.; Meis, J. F.; Jackson, B.; Chiller, T.; Litvintseva, A. P. Simultaneous Emergence of Multidrug-Resistant *Candida auris* on 3 Continents Confirmed by Whole-Genome Sequencing and Epidemiological Analyses. *Clin. Infect. Dis.* **2017**, *64*, 134–140.
- (18) Escandón, P.; Chow, N. A.; Caceres, D. H.; Gade, L.; Berkow, E. L.; Armstrong, P.; Rivera, S.; Misas, E.; Duarte, C.; Moulton-Meissner, H. Molecular Epidemiology of *Candida auris* in Colombia Reveals a Highly Related, Countrywide Colonization with Regional Patterns in Amphotericin B Resistance. *Clin. Infect. Dis.* **2019**, *68*, 15–21.
- (19) Chowdhary, A.; Prakash, A.; Sharma, C.; Kordalewska, M.; Kumar, A.; Sarma, S.; Tarai, B.; Singh, A.; Upadhyaya, G.; Upadhyay, S.; Yadav, P.; Singh, P. K.; Khillan, V.; Sachdeva, N.; Perlin, D. S.; Meis, J. F. A Multicentre Study of Antifungal Susceptibility Patterns among 350 *Candida auris* Isolates (2009–17) in India: Role of the ERG11 and FKS1 Genes in Azole and Echinocandin Resistance. *J. Antimicrob. Chemother.* 2018, 73, 891–899.
- (20) Berkow, E. L.; Lockhart, S. R. Activity of CD101, a Long-Acting Echinocandin, against Clinical Isolates of *Candida auris*. *Diagn. Microbiol. Infect. Dis.* **2018**, *90*, 196–197.
- (21) Franci, G.; Falanga, A.; Galdiero, S.; Palomba, L.; Rai, M.; Morelli, G.; Galdiero, M. Silver Nanoparticles as Potential Antibacterial Agents. *Molecules* **2015**, *20*, 8856–8874.
- (22) Mallakpour, S.; Abdolmaleki, A.; Borandeh, S.; Sabzalian, M. R. One Pot Fabrication of Optically Active and Efficient Antibacterial Poly (Amide-Benzimidazole-Imide)/Ag Bionanocomposite. *J. Polym. Res.* **2015**, 22, 129.
- (23) Gordon, T.; Perlstein, B.; Houbara, O.; Felner, I.; Banin, E.; Margel, S. Synthesis and Characterization of Zinc/Iron Oxide Composite Nanoparticles and Their Antibacterial Properties. *Colloids Surf.*, A 2011, 374, 1–8.
- (24) Kanagasubbulakshmi, S.; Kadirvelu, K. Green Synthesis of Iron Oxide Nanoparticles Using *Lagenaria Siceraria* and Evaluation of Its Antimicrobial Activity. *Def. Life Sci. J.* **2017**, *2*, 422–427.
- (25) Jadhav, M. S.; Kulkarni, S.; Raikar, P.; Barretto, D. A.; Vootla, S. K.; Raikar, U. Green Biosynthesis of CuO & Ag—CuO Nanoparticles from *Malus Domestica* Leaf Extract and Evaluation of Antibacterial, Antioxidant and DNA Cleavage Activities. *New J. Chem.* **2018**, *42*, 204—213.
- (26) Karthik, K.; Dhanuskodi, S.; Kumar, S. P.; Gobinath, C.; Sivaramakrishnan, S. Microwave Assisted Green Synthesis of MgO Nanorods and Their Antibacterial and Anti-Breast Cancer Activities. *Mater. Lett.* **2017**, *206*, 217–220.
- (27) Martinez, L. R.; Han, G.; Chacko, M.; Mihu, M. R.; Jacobson, M.; Gialanella, P.; Friedman, A. J.; Nosanchuk, J. D.; Friedman, J. M. Antimicrobial and Healing Efficacy of Sustained Release Nitric Oxide

- Nanoparticles against Staphylococcus aureus Skin Infection. J. Invest. Dermatol. 2009, 129, 2463–2469.
- (28) Bahadar, H.; Maqbool, F.; Niaz, K.; Abdollahi, M. Toxicity of Nanoparticles and an Overview of Current Experimental Models. *Iran Biomed J.* **2016**, *20*, 1–11.
- (29) Wang, X.; Liu, X.; Chen, J.; Han, H.; Yuan, Z. Evaluation and Mechanism of Antifungal Effects of Carbon Nanomaterials in Controlling Plant Fungal Pathogen. *Carbon* **2014**, *68*, 798–806.
- (30) Benincasa, M.; Pacor, S.; Wu, W.; Prato, M.; Bianco, A.; Gennaro, R. Antifungal Activity of Amphotericin B Conjugated to Carbon Nanotubes. *ACS Nano* **2011**, *5*, 199–208.
- (31) Miao, H.; Teng, Z.; Wang, C.; Chong, H.; Wang, G. Recent Progress in Two-Dimensional Antimicrobial Nanomaterials. *Chem. Eur. J.* **2019**, 25, 929–944.
- (32) Zhu, Y.; Murali, S.; Cai, W.; Li, X.; Suk, J. W.; Potts, J. R.; Ruoff, R. S. Graphene and Graphene Oxide: Synthesis, Properties, and Applications. *Adv. Mater.* **2010**, *22*, 3906–3924.
- (33) Mallakpour, S.; Abdolmaleki, A.; Borandeh, S. Covalently Functionalized Graphene Sheets with Biocompatible Natural Amino Acids. *Appl. Surf. Sci.* **2014**, *307*, 533–542.
- (34) Mohammed, H.; Kumar, A.; Bekyarova, E.; Al-Hadeethi, Y. M.; Zhang, X.; Chen, M.; Ansari, S.; Cochis, A.; Rimondini, L. Antimicrobial Mechanisms and Effectiveness of Graphene and Graphene-Functionalized Biomaterials. A Scope Review. *Front. Bioeng. Biotechnol.* **2020**, *8*, 465.
- (35) Yang, Y.; Liu, T.; Cheng, L.; Song, G.; Liu, Z.; Chen, M. MoS<sub>2</sub>-Based Nanoprobes for Detection of Silver Ions in Aqueous Solutions and Bacteria. *ACS Appl. Mater. Interfaces* **2015**, *7*, 7526–7533.
- (36) Zhang, W.; Mou, Z.; Wang, Y.; Chen, Y.; Yang, E.; Guo, F.; Sun, D.; Wang, W. Molybdenum Disulfide Nanosheets Loaded with Chitosan and Silver Nanoparticles Effective Antifungal Activities: *In Vitro* and *in Vivo*. *Mater. Sci. Eng. C* **2019**, *97*, 486–497.
- (37) Kurapati, R.; Muzi, L.; de Garibay, A. P. R.; Russier, J.; Voiry, D.; Vacchi, I. A.; Chhowalla, M.; Bianco, A. Enzymatic Biodegradability of Pristine and Functionalized Transition Metal Dichalcogenide MoS<sub>2</sub> Nanosheets. *Adv. Funct. Mater.* **2017**, *27*, 1605176.
- (38) Roy, S.; Mondal, A.; Yadav, V.; Sarkar, A.; Banerjee, R.; Sanpui, P.; Jaiswal, A. Mechanistic Insight into the Antibacterial Activity of Chitosan Exfoliated MoS<sub>2</sub> Nanosheets: Membrane Damage, Metabolic Inactivation, and Oxidative Stress. *ACS Appl. Bio Mater.* **2019**, *2*, 2738–2755.
- (39) Pandit, S.; Karunakaran, S.; Boda, S. K.; Basu, B.; De, M. High Antibacterial Activity of Functionalized Chemically Exfoliated MoS<sub>2</sub>. ACS Appl. Mater. Interfaces **2016**, *8*, 31567–31573.
- (40) Cao, F.; Ju, E.; Zhang, Y.; Wang, Z.; Liu, C.; Li, W.; Huang, Y.; Dong, K.; Ren, J.; Qu, X. An Efficient and Benign Antimicrobial Depot Based on Silver-Infused MoS<sub>2</sub>. ACS Nano **2017**, *11*, 4651–4659.
- (41) Liu, X.; Duan, G.; Li, W.; Zhou, Z.; Zhou, R. Membrane Destruction-Mediated Antibacterial Activity of Tungsten Disulfide (WS<sub>2</sub>). RSC Adv. 2017, 7, 37873–37880.
- (42) Rasool, K.; Helal, M.; Ali, A.; Ren, C.; Gogotsi, Y.; Mahmoud, K. Antibacterial Activity of  ${\rm Ti_3C_2T_x}$  MXene. ACS Nano 2016, 10, 3674–3684
- (43) Bang, G. S.; Cho, S.; Son, N.; Shim, G. W.; Cho, B.-K.; Choi, S.-Y. DNA-Assisted Exfoliation of Tungsten Dichalcogenides and Their Antibacterial Effect. *ACS Appl. Mater. Interfaces* **2016**, *8*, 1943–1950.
- (44) Das, B.; Khan, M. I.; Jayabalan, R.; Behera, S. K.; Yun, S.-I.; Tripathy, S. K.; Mishra, A. Understanding the Antifungal Mechanism of Ag@ ZnO Core-Shell Nanocomposites against *Candida krusei. Sci. Rep.* **2016**. *6*, 465.
- (45) Debnath, A.; Saha, S.; Li, D. O.; Chu, X. S.; Ulissi, Z. W.; Green, A. A.; Wang, Q. H. Elimination of Multidrug-Resistant Bacteria by Transition Metal Dichalcogenides Encapsulated by Synthetic Single-Stranded DNA. ACS Appl. Mater. Interfaces 2021, 13, 8082–8094.
- (46) Alimardani, V.; Abolmaali, S. S.; Borandeh, S. Antifungal and Antibacterial Properties of Graphene-Based Nanomaterials: A Mini-Review. *J. Nanostruct.* **2019**, *9*, 402–413.

- (47) Sawangphruk, M.; Srimuk, P.; Chiochan, P.; Sangsri, T.; Siwayaprahm, P. Synthesis and Antifungal Activity of Reduced Graphene Oxide Nanosheets. *Carbon* **2012**, *50*, 5156–5161.
- (48) Bhatt, V. K.; Patel, M.; Pataniya, P. M.; Iyer, B. D.; Sumesh, C.; Late, D. J. Enhanced Antifungal Activity of WS<sub>2</sub>/ZnO Nanohybrid against *Candida albicans. ACS Biomater. Sci. Eng.* **2020**, *6*, 6069–6075.
- (49) Amato, D. V.; Amato, D. N.; Blancett, L. T.; Mavrodi, O. V.; Martin, W. B.; Swilley, S. N.; Sandoz, M. J.; Shearer, G.; Mavrodi, D. V.; Patton, D. L. A Bio-Based Pro-Antimicrobial Polymer Network via Degradable Acetal Linkages. *Acta Biomater.* **2018**, *67*, 196–205.
- (50) Fan, X.; Ngo, H.; Wu, C. Natural and Bio-Based Antimicrobials: A Review. In *Natural and Bio-Based Antimicrobials for Food Applications*; ACS Symposium Series: 2018; pp. 1–24.
- (51) Shankar, S.; Rhim, J.-W. Preparation of Sulfur Nanoparticle-Incorporated Antimicrobial Chitosan Films. *Food Hydrocolloids* **2018**, 82, 116–123.
- (52) Park, Y.-K.; Kim, M.-H.; Park, S.-C.; Cheong, H.-S.; Jang, M.-K.; Nah, J.-W.; Hahm, K.-S. Investigation of the Antifungal Activity and Mechanism of Action of LMWS-Chitosan. *J. Microbiol. Biotechnol.* **2008**, *18*, 1729–1734.
- (53) Yien, L.; Zin, N. M.; Sarwar, A.; Katas, H. Antifungal Activity of Chitosan Nanoparticles and Correlation with Their Physical Properties. *Int. J. Biomater.* **2012**, *2012*, 632698.
- (54) Sundaram, J.; Pant, J.; Goudie, M. J.; Mani, S.; Handa, H. Antimicrobial and Physicochemical Characterization of Biodegradable, Nitric Oxide-Releasing Nanocellulose—Chitosan Packaging Membranes. J. Agric. Food Chem. 2016, 64, 5260—5266.
- (55) Li, C.; Wang, X.; Chen, F.; Zhang, C.; Zhi, X.; Wang, K.; Cui, D. The Antifungal Activity of Graphene Oxide—Silver Nanocomposites. *Biomaterials* **2013**, *34*, 3882—3890.
- (56) Hu, Y.; Qi, X.; Sun, H.; Lu, Y.; Hu, Y.; Chen, X.; Liu, K.; Yang, Y.; Mao, Z.; Wu, Z.; Zhou, X. Photodynamic Therapy Combined with Antifungal Drugs against Chromoblastomycosis and the Effect of ALA-PDT on *Fonsecaea in Vitro*. *PLoS Neglected Trop. Dis.* **2019**, *13*, No. e0007849.
- (57) Zhang, Y.; Huang, P.; Wang, D.; Chen, J.; Liu, W.; Hu, P.; Huang, M.; Chen, X.; Chen, Z. Near-Infrared-Triggered Antibacterial and Antifungal Photodynamic Therapy Based on Lanthanide-Doped Upconversion Nanoparticles. *Nanoscale* **2018**, *10*, 15485–15495.
- (58) Nam, D.; Lee, J.-U.; Cheong, H. Excitation Energy Dependent Raman Spectrum of MoSe<sub>2</sub>. Sci. Rep. **2015**, *S*, 17113.
- (59) Balasingam, S. K.; Lee, J. S.; Jun, Y. Few-Layered MoSe<sub>2</sub> Nanosheets as an Advanced Electrode Material for Supercapacitors. *Dalton Trans.* **2015**, *44*, 15491–15498.
- (60) Wu, H.; Wu, Y.; Chen, X.; Ma, Y.; Xu, M.; Wei, W.; Pan, J.; Xiong, X. Rational Design and Preparation of Few-Layered MoSe<sub>2</sub> Nanosheet@ C/TiO<sub>2</sub> Nanobelt Heterostructures with Superior Lithium Storage Performance. *RSC Adv.* **2016**, *6*, 23161–23168.
- (61) Han, S.; Liu, K.; Hu, L.; Teng, F.; Yu, P.; Zhu, Y. Superior Adsorption and Regenerable Dye Adsorbent Based on Flower-Like Molybdenum Disulfide Nanostructure. *Sci. Rep.* **2017**, *7*, 43599.
- (62) Zheng, C.; Chen, C.; Chen, L.; Wei, M. A CMK-5-Encapsulated MoSe<sub>2</sub> Composite for Rechargeable Lithium-Ion Batteries with Improved Electrochemical Performance. *J. Mater. Chem. A* **2017**, *5*, 19632–19638.
- (63) Liu, H.; Hu, H.; Wang, J.; Niehoff, P.; He, X.; Paillard, E.; Eder, D.; Winter, M.; Li, J. Hierarchical Ternary MoO<sub>2</sub>/MoS<sub>2</sub>/Heteroatom-Doped Carbon Hybrid Materials for High-Performance Lithium-Ion Storage. *ChemElectroChem* **2016**, *3*, 922–932.
- (64) Liu, J.; Li, F.; Zheng, J.; Li, B.; Zhang, D.; Jia, L. Redox/NIR Dual-Responsive MoS<sub>2</sub> for Synergetic Chemo-Photothermal Therapy of Cancer. *J. Nanobiotechnol.* **2019**, *17*, 78.
- (65) Jeyaraj Pandian, C.; Palanivel, R.; Dhanasekaran, S. Screening Antimicrobial Activity of Nickel Nanoparticles Synthesized Using *Ocimum sanctum* Leaf Extract. *J. Nanopart.* **2016**, 2016, 4694367.
- (66) Yu, Z.; Li, Q.; Wang, J.; Yu, Y.; Wang, Y.; Zhou, Q.; Li, P. Reactive Oxygen Species-Related Nanoparticle Toxicity in the Biomedical Field. *Nanoscale Res. Lett.* **2020**, *15*, 115.

(67) Chauhan, R.; Loonker, S. Synthesis, Characterization and Biological Evaluation of Chitosan Epoxy N-Methyl Piperazine as Antimicrobial Agent. *Int. J. Pharm. Sci. Rev. Res.* **2017**, 266–270. (68) Wu, R.; Ou, X.; Tian, R.; Zhang, J.; Jin, H.; Dong, M.; Li, J.; Liu, L. Membrane Destruction and Phospholipid Extraction by Using Two-Dimensional MoS<sub>2</sub> Nanosheets. *Nanoscale* **2018**, *10*, 20162–20170.

## **□** Recommended by ACS

### Elimination of Multidrug-Resistant Bacteria by Transition Metal Dichalcogenides Encapsulated by Synthetic Single-Stranded DNA

Abhishek Debnath, Qing Hua Wang, et al.

FEBRUARY 11, 2021

ACS APPLIED MATERIALS & INTERFACES

READ 🗹

# Phase-Dependent MoS<sub>2</sub> Nanoflowers for Light-Driven Antibacterial Application

Chinmaya Mutalik, Tsung-Rong Kuo, et al.

JUNE 02, 2021

ACS SUSTAINABLE CHEMISTRY & ENGINEERING

READ 🗹

# Amino Acid-Functionalized ${\rm MoS}_2$ Quantum Dots for Selective Antibacterial Activity

Avijit Mondal and Mrinmoy De

NOVEMBER 30, 2021

ACS APPLIED NANO MATERIALS

READ 🗹

# Laser-Induced $MoO_x$ /Sulfur-Doped Graphene Hybrid Frameworks as Efficient Antibacterial Agents

Yong Yang, Yafei Zhang, et al.

JANUARY 22, 2021

LANGMUIR

READ 🗹

Get More Suggestions >